

**Fabrication and modelling of an all-printed
PEDOT:PSS supercapacitor on a commercial paper**

by

Dan Sik Yoo

B.A.Sc., Sungkyunkwan University, 2000

A THESIS SUBMITTED IN PARTIAL FULFILLMENT
OF THE REQUIREMENTS FOR THE DEGREE OF

MASTER OF APPLIED SCIENCE

in

THE FACULTY OF GRADUATE STUDIES

(Electrical and Computer Engineering)

The University Of British Columbia

(Vancouver)

June 2010

© Dan Sik Yoo, 2010

Abstract

Supercapacitors demonstrate substantial improvement in charge storage capability compared to the conventional capacitors. With the emergence of printed electronics such as RFID tags, smart cards, electronic paper, and wearable electronics, printed energy storage devices are desirable. Therefore, a flexible and printable supercapacitor with a PEDOT:PSS electrode is fabricated with inkjet micropatterning technology. Electroanalytical measurement techniques are employed to characterize the performance of the printed supercapacitor. It has been found that addition of the surfactant (Triton X-100) increases the porosity of the PEDOT:PSS electrode. A volume capacitance of 9.36 F/cm^3 (adding surfactant) and 9.09 F/cm^3 (without adding surfactant) are measured with cyclic voltammetry. The two devices have different capacitor charging times, e.g., 50.46 s for electrode added surfactant and 112.9 s for the electrode without adding surfactant.

In order to investigate the rate limiting factors of capacitor charging, electrochemical impedance measurements and equivalent circuit modelling is utilized. Instead of using a constant phase element (CPE), a multiple time constant model

is proposed in order to explain the physical origin of the distributed time constant behaviour. Thickness variation of the PEDOT:PSS electrode is assumed as a primary reason for the distributed time constants and thus actual thickness variation is incorporated in the modelling. Data fitting with the measured impedance are consistent with this assumption. However, it also has been found that there are more factors distributing capacitances than just variations in thickness. A log-normal distribution function (LNDF) is utilized in order to further investigate the relationship between the distributed capacitance and the capacitor charging. It is found that the capacitance distribution likely influence the charging.

Previous experimental results demonstrate that the distributed capacitance is the physical cause of the distributed time constant behaviour in electrochemical impedance measurement. However, this is the first analytical report proving the relationship between the distributed time constant behaviour and a thickness dependent capacitance distribution.

Table of Contents

Abstract	ii
Table of Contents	iv
List of Tables	vi
List of Figures	vii
Acknowledgments	x
1 Introduction	1
1.1 Supercapacitor fundamentals	3
1.2 Commercial applications	7
1.3 Thesis overview	10
2 Supercapacitor electrode fabrication using inkjet printing technology	12
2.1 Motivation of using inkjet printing technology	13
2.2 Characterization of the printing parameters	16
2.3 Equipment setup and electrode printing	18

3 Experiments and results	23
3.1 Porosity measurements with AFM, FESEM, and BET technique	24
3.2 Ionic conductivity	27
3.3 Cyclic voltammetry	30
3.4 Electrochemical impedance spectroscopy	34
4 Multiple time constant model	42
4.1 The origin of the CPE response	43
4.2 The origin of capacitance distribution of the PEDOT:PSS electrode	46
4.3 Multiple time constant modelling	49
4.4 Data fitting of the multiple time constant model	56
5 Conclusions	65
Bibliography	68
Appendices	75
A Design of the printing nozzle housing	76
B Nozzle maintenance tips	79

List of Tables

3.1	Volume capacitance decreases as scan rate increases, WT and NT refer to electrodes with Triton X-100 and without Triton X-100 respectively.	24
3.2	Volume capacitances calculated from the EIS data for both WT and NT at different scan rates.	40
4.1	The average thickness of the two PEDOT:PSS electrodes (WT and NT) and bare paper roughness along five different lines.	47
4.2	Experiment and modelling data comparison. C , σ_i , R_s , and R_f refer to the capacitance, ionic conductivity, solution resistance, and faradaic resistance respectively	62

List of Figures

1.1	The energy storage mechanism of a regular capacitor.	3
1.2	A equivalent circuit of the supercapacitor electrode. R_e , C , R_i , and R_s represent electrical resistance, capacitance, ionic resistance, and solution resistance respectively.	5
1.3	The Ragone plot for various energy storage devices. Adapted from [10]-[11].	8
2.1	Dispensing frequency and continuous line patterning a) 333 Hz b) 833 Hz c) 1666 Hz d) 2333 Hz e) 3000 Hz.	18
2.2	a) The inkjet printer stage setup b) the paper attachment on the substrate heater c) the substrate heater and the silicon gasket. . . .	19
2.3	PEDOT:PSS deposition on commercially available letter size papers which are showing different particle agglomeration and penetration. #1-1, #2-1, and #3-1 are from Husky xerocopy (Canada), Hansol paper (Korea), and Korea paper (Korea), respectively. . . .	21
2.4	Electrode pattern on a commercial paper (whitestone, Neenah paper company, USA).	22

3.1	AFM images for both WT and NT samples.	26
3.2	Cross section images of the electrode from FESEM.	27
3.3	Ionic conductivity test apparatus and the equivalent circuit of the ionic conductivity measurement. WE, RE, and CE refer to working electrode, reference electrode, and counter electrode respectively. The sample is placed at the center, clamped between two circular cups.	28
3.4	The cyclic voltammetry of the PEDOT:PSS electrodes at 10 mV/s (top) and 1 mV/s (bottom) scan rates.	32
3.5	The cyclic voltammetry of the PEDOT:PSS electrodes at 0.1 mV/s scan rate.	33
3.6	a) Electrode with aluminum foil substrate b) coil shape platinum wire and stainless steel sheet piece.	36
3.7	Abnormal impedance response without stainless steel wire connection to RE at high frequency.	37
3.8	The EIS three electrode cell setup.	38
3.9	Volumetric capacitance vs. frequency plot from the EIS and its corresponding scan rate in the CV.	39
4.1	Microscope image of the PEDOT:PSS electrode surface.	45
4.2	a) The deposition direction (from top lines to bottom lines) of the PEDOT:PSS electrode b) the thickness scan direction of the PEDOT:PSS electrode.	47

4.3	Thickness profile for both WT and NT electrodes at #3 (center) position scan.	48
4.4	The total thickness deviation of the PEDOT:PSS electrode which is measured from scan #1 to #5.	50
4.5	The simple drawing of the multiple thickness electrode (top) and equivalent circuit for one section of the electrode (bottom).	51
4.6	The three electrode EIS measurement setup for measuring solution resistance. A stainless steel sheet (SSS) is used as a working electrode. WE, RE, and CE refer to the working electrode, reference electrode, and counter electrode respectively.	52
4.7	The Bode plot of the NT electrode.	57
4.8	The Nyquist plot of the NT electrode.	58
4.9	The Bode plot of the WT electrode.	59
4.10	The Nyquist plot of the WT electrode.	60
4.11	Phase angle response with different σ_t values.	61
A.1	Design and assembly of the inkjet printing nozzle housing.	77

Acknowledgments

I would like to give my special thanks to my supervisor, Professor John D. Maden, for giving me an opportunity to join the lab and supporting me throughout my studies. He always inspired me with his great knowledge and experience and also gave me clear guidance and advice. I also would like to thank Professor Konrad Walus, who helped me to finalize the experiments and the project. The progress of this research would have not been possible without his advice and encouragement.

I thank Professor Andre Ivanov for giving me a chance to join UBC and having a chance to explore academia. Many thanks to Dr. Arash Takshi for helping me out when I first started the supercapacitor project. I would have had many difficulties in a new environment without your help. Many thanks to all the lab members for helpful comments, discussions, and cooperation. I greatly benefitted from their theoretical insights and experiences.

I deeply appreciate my wife (Ji Hey Jung) for her sacrifice to support me throughout my Master's. I also thank my daughter (Jean Ruhiyyih Yoo) for grow-

ing without any problems and giving me joy and energy in life.

Chapter 1

Introduction

Within the last decade, we have seen incredible innovations in portable electronic devices such as mobile phones, smartphones, MP3 players, digital cameras, etc. However, recent trends in portable devices also brought an issue to the rechargeable lithium-ion battery. By integrating many features in a portable device, the battery also has to cope with high power consumption. This new challenge may shorten life time of the battery or it may also cause performance failure. One of the main obstacles in battery design is maintaining voltage levels of the battery. However, due to the high current that is often required, it has become difficult to sustain a stable voltage level. When the voltage drops below an operational range, then the internal passivation layer of the lithium battery starts to break down and induces considerable leakage current inside the battery. These kinds of constant leakage currents shorten the battery life time.

Supercapacitors can be a promising solution for increased power demands in consumer electronics devices. By placing supercapacitors in parallel with the batteries, the dramatic voltage drops can be prevented and it can extend life time of the battery. Whenever a device needs high power, the supercapacitors will fill the increased demand instead of a battery. The supercapacitor will then be recharged in a short time[1].

Supercapacitors have several names such as electrochemical double layer capacitor (EDLC), ultracapacitor, and pseudocapacitor. They have remarkably high specific capacitance (capacitance per unit mass) and energy density compared to conventional capacitors. If the supercapacitors can provide similar energy density to batteries, this would provide significant value to many devices. However, due to the lower energy densities but high power supply capabilities, supercapacitors are getting attention primarily as a complementary energy source to batteries[2].

The unique features (low cost, thin, lightweight, and also flexible) of the printed energy storage devices are getting great attention with the emergence of printed electronics such as RFID tags, smart cards, electronic paper, and wearable electronics. In this thesis, a rectangular (12 mm x 12 mm) PEDOT:PSS supercapacitor is fabricated using inkjet micropatterning and characterized by using electroanalytical methods

1.1 Supercapacitor fundamentals

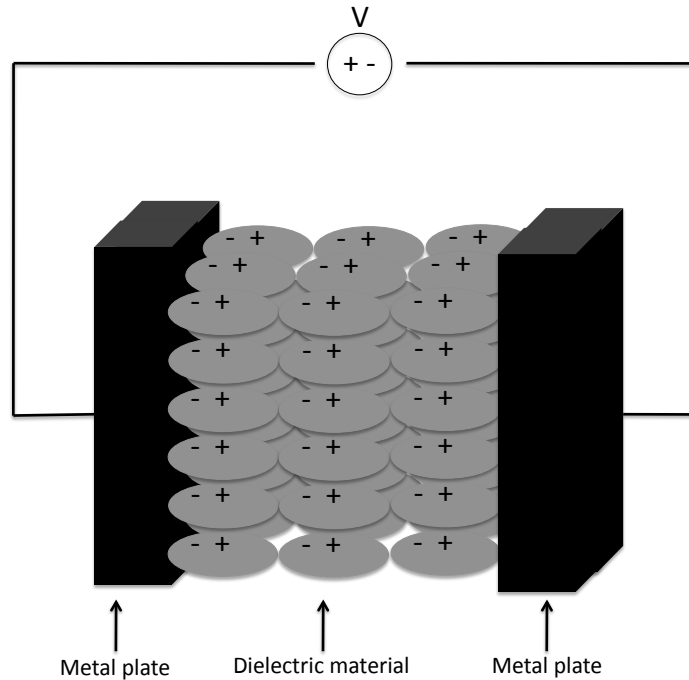


Figure 1.1: The energy storage mechanism of a regular capacitor.

The basics of the capacitor are briefly reviewed before we discuss the supercapacitor fundamentals. The conventional capacitor consists of two metal plates which are sandwiching a dielectric material as shown in Figure 1.1. When a voltage is applied between two metal plates, charges separate from one side of the metal plate and accumulate at the other side of the metal plate. The capacitance of a simple capacitor is proportional to the area of the contact plates and the per-

mittivity of the dielectric. The capacitance of a parallel plate capacitor is

$$C = \epsilon_r \cdot \epsilon_0 \cdot \frac{A}{d}, \quad (1.1)$$

where C , ϵ_r , ϵ_0 , A , and d are the capacitance, relative permittivity, electric constant, the area the metal plate, and the distance between two plates.

Supercapacitors are a unique kind of capacitor. Whereas a common capacitor stores charges at only the surface of the metal plate, supercapacitors store charges through the whole volume of the electrode due to the porous nature of the electrode materials. The Figure 1.2 describes a equivalent circuit of one supercapacitor electrode. When voltage is applied to the electrode, ions penetrate inside the electrode and charge the electrode. When the electrode is positively charged, the electrode repels positive ions and attracts negative ions, whereas a negatively charged electrode behaves in opposite way and charges the entire volume of the electrode.

Supercapacitors are normally divided into two groups according to their energy storage mechanism. The first one only uses electrostatic charge accumulation between the electrode and the electrolyte rather than using electrochemical reactions. Carbon materials belong to this group and this is the reason why these supercapacitors are commonly classed as electrochemical double layer capacitors (EDLC). The second mechanism utilizes charge transfer reactions which are ob-

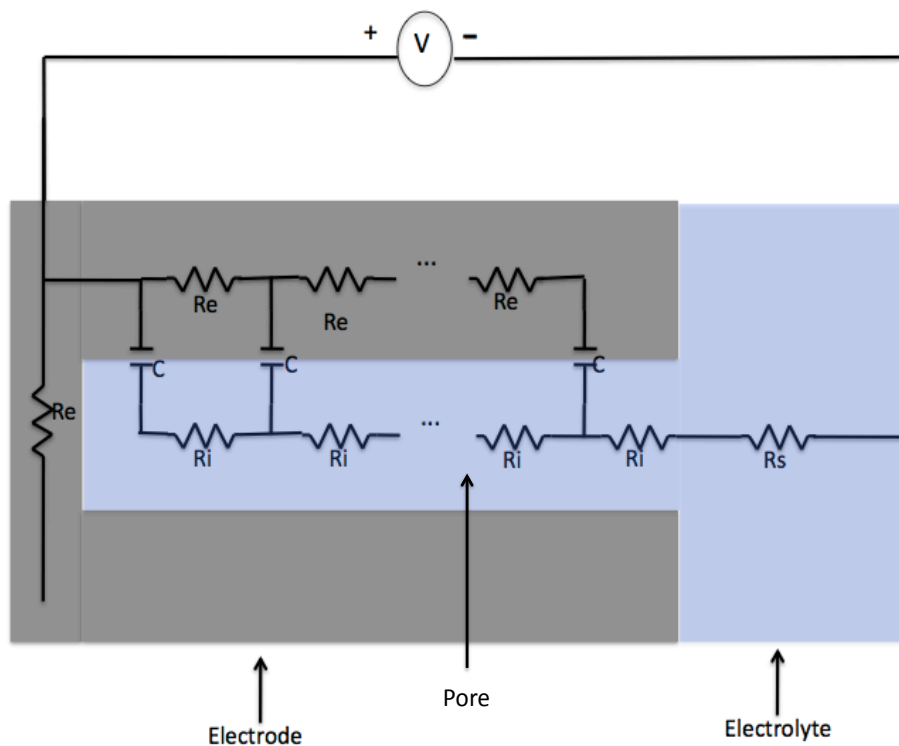


Figure 1.2: A equivalent circuit of the supercapacitor electrode. R_e , C , R_i , and R_s represent electrical resistance, capacitance, ionic resistance, and solution resistance respectively.

served in electro-active materials (metal oxides or conducting polymers). The capacitance values for these materials are reported to be much higher than EDLC materials.

Supercapacitors demonstrate substantial improvement in charge storage capa-

bility compared to the conventional capacitors because the distance between the electrode and electrolyte ions are on the order of nanometers (~ 1 nm) in the electrical double layer [3]-[4]. The amount of charge stored at the surface of the electrode is mainly determined by the accessible surface area. For porous materials which are used in supercapacitor electrodes, the charge/discharge processes take place throughout the entire volume and not only at the surface of the material.

Most of the energy stored in carbon materials is in the electrostatic charge separation rather than charge transfer reaction[9]. Carbon is one of the commonly used materials for supercapacitors because of the high surface area, low material cost, processability, and chemical/temperature stability. Additionally, the activation procedures that control carbon porosity are well understood and developed. Activated carbon devices have demonstrated a wide range specific capacitances (100 - 400 F/g) depending on the surface area (m^2/g), pore size distribution, and surface double layer capacitance ($\mu\text{F}/\text{cm}^2$) [5].

There is another class of electrochemical energy storage supercapacitors which utilize pseudo-capacitance. Unlike the EDLC, pseudo-capacitance utilizes the charge transfer reactions between the electrode and the electrolyte associated with electrosorption and surface redox processes with high surface area of the electrode. Metal oxide materials (e.g. RuO_2 , MnO_2) or conducting polymers (polypyrrole, polyaniline, polythiophene derivatives) store charges with such faradaic processes but the electrical behaviour is like that of a capacitor. Whereas the capaci-

tance of ideal EDLC is constant, the pseudo-capacitance is usually dependent on potential. However, almost constant capacitance response over the full voltage window (~ 1.4 V) has been reported for RuO_2 . In addition to the constant capacitance response, it also demonstrates high specific capacitance (650 F/g)[5], great cyclability and high conductivity [6]. However, due to the high cost of the RuO_2 , it has mostly been used in military applications.

Conducting polymers are less stable than RuO_2 . However due to their significantly lower cost, conducting polymers are getting attention as a substitute for supercapacitor material. Conducting polymers can be charged positively or negatively with inserted ions and pseudo capacitance arises with the faradaic charge transfer reaction[7]. K. R. Prasad and N. Munichandraiah have demonstrated specific capacitance of 1300 F/g with polyaniline (PANI) on a stainless steel substrate[8].

1.2 Commercial applications

Since their first commercialization as backup power supply for computer memory in 1978 (NEC company, Japan), supercapacitors have been used in applications where power density is a higher priority than energy density. As shown in Figure 1.3, supercapacitors are filling the gap between batteries and conventional capacitors. The energy density of the supercapacitor (~ 10 Wh/kg) is fairly high compared to a conventional capacitor (~ 0.05 Wh/kg). However it is only about

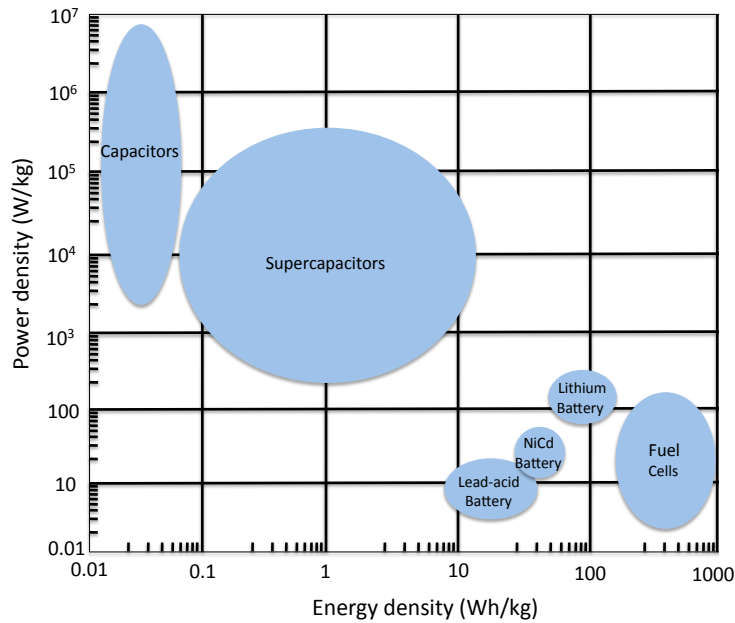


Figure 1.3: The Ragone plot for various energy storage devices. Adapted from [10]-[11].

one-tenth that of a battery. The specific power of supercapacitors is much higher than batteries. As a result, supercapacitors can deliver energy in a short time but they cannot provide a lot of energy, whereas batteries can provide a considerable quantities of energy but powering of a high power device is not an optimal application for battery. Supercapacitors can supply large amounts of charge very quickly and can be recharged in short times. Supercapacitors demonstrate great cyclic performance. Battery can only be charged/discharged approximately one

thousand times. However, supercapacitors generally show only little degradation after thousands of cycles. Supercapacitors also demonstrate very low internal resistance, low heating levels, and good safety standards. Batteries supply steady voltage in the usable voltage range, whereas the voltage of a supercapacitor drops linearly from the beginning of discharge and this hinders supercapacitors from providing full charge. About 75 % of the total energy of supercapacitors can be utilized by using a DC-DC converter [10].

The hybrid electrical vehicle (HEV) power source application has substantial potential as a new market for supercapacitors. By utilizing the complementary properties of batteries and supercapacitors, it can greatly enhance the HEV performance. Supercapacitors have great advantages of supplying bursts of power and charging very quickly. For instance, supercapacitors can deliver the power when vehicles need high power (acceleration or hill climbing). They also can be utilized to capture the regenerative braking energy[12].

As they first found their application in backup power for computer memory, backup power sources for the consumer electronic products are one of the biggest markets for supercapacitors. For instance, we can find supercapacitor application in satellite TV (TV-channel setting, clock time), car audio systems (radio station memory), coffee machines (protect programmed functions), and programmable pocket calculator among others[10].

1.3 Thesis overview

In chapter 2, inkjet micropatterning technology is introduced and advantages and limitations are discussed in various applications. All the parameters (voltage, pulse length and frequency) determining droplet formation and deposition speed are defined. The detailed fabrication procedures of the PEDOT:PSS electrode are also described in the chapter.

In chapter 3, electroanalytical measurement techniques, e.g., ionic conductivity measurement, cyclic voltammetry (CV), and electrochemical impedance spectroscopy (EIS) are employed to characterize the PEDOT:PSS electrode. The ionic conductivity measurements suggest that the surfactant Triton - X100, increases the porosity of the PEDOT:PSS electrode. In the CV measurements, varying scan rates (10 mV/s, 1 mV/s, and 0.1 mV/s) are applied to investigate the relationship between increased porosity and the capacitance associated with the addition of Triton X-100. EIS is used to measure the impedance of the system over a range of frequencies in order to characterize energy storage behaviour of the PEDOT:PSS.

In chapter 4, a multiple time-constant model is proposed in order to explain the physical origin of the constant phase element (CPE) behaviour in the EIS measurements. Although it does not help to identify the origin of the response, the CPE is widely used in electrochemical impedance modelling in order to represent time constant distributions in an equivalent circuit. The thickness variation of

the printed PEDOT:PSS was found to be the primary physical origin of the capacitance distribution. However, there could be other possibilities that may lead to a distributed capacitance. All the modelling parameters (ionic conductivity, solution conductivity, and capacitance) are also compared with the experimental data.

Chapter 2

Supercapacitor electrode fabrication using inkjet printing technology

This chapter details the inkjet micropatterning technology that is utilized to fabricate the device studied in this thesis. In Section 2.1, we briefly introduce the characteristics of inkjet printing as a fabrication technology and discuss the advantages and limitations in various applications. In Section 2.2, recent research reports that investigate the relationship between droplet formation and control parameters are introduced. We also describe features of key parameters (voltage, pulse length, frequency) that affect droplet shape and speed of deposition. In Section 2.3, we describe the inkjet system setup and electrode printing procedures.

2.1 Motivation of using inkjet printing technology

Inkjet printing technology is most commonly used for document printing onto paper. In addition, it also has widespread commercial applications in printing product information onto cans or bottles. However, in recent years, the micro patterning capability of inkjet printing technology coupled with conducting polymers or novel nanoparticles is also getting great attention[13]-[14].

Drop-on-demand (DOD) printers eject ink droplets when and where they are needed to create patterns on a substrate. This approach eliminates the complexity of drop charging and deflection hardware, as well as the inherent unreliability of ink recirculation systems required for continuous inkjet technology. Thermal and piezoelectric printing technologies are competing with each other in the market with this mode. Thermal inkjet printers have occupied most of the low cost office printer market. However, this system only can work with highly tailored inks. If other inks are used in thermal printers their performance/life can be degraded radically due to the vaporization process, whereas the piezoelectric inkjet systems do not modify the ink properties and have the capability to dispense a wide range of solutions. Thus, piezoelectric inkjet printing technology has become the main choice for experimental DOD systems.

Piezoelectric printers are categorized by the deformation methods (squeeze, bend, push and shear[15]-[16]) of the piezoelectric ceramic used in the device.

The squeeze mode is used for our experimental apparatus. The core of the device consists of a glass capillary which is surrounded by a tubular piezoelectric actuator. The actuator is controlled by the electrostatic field and its squeezing actuation creates a pressure pulse inside the glass capillary. A small amount of liquid is ejected from the orifice due to the pressure pulse and it forms a uniform droplet.

Unique fabrication features of high resolution inkjet micropatterning is attracting great attention[17]-[18]. Direct material deposition is a more environmentally friendly process because it is not based on subtractive lithography steps that waste significant portion of materials. Furthermore, less material and simple fabrication steps yield a lower cost process. Organic and biological materials that are not compatible with semiconductor processes can also be deposited. Manufacturing on flexible substrates is also possible since the process is low temperature. In recent years, there has been extensive research and promising results that utilize inkjet printing technology in various applications.

Inkjet microdispensing technology is adaptable to high density DNA array fabrication [19]. The capability of dispensing nano to picoliter volumes onto the specific DNA test site is a significant advantage of utilizing inkjet technology in biomedical arrays. Liquid delivery capability of a small volume with high speed features of inkjet microdispensing technology has promising potential of combinatorial chemistry [20]. Whereas, chemical compatibility with a wide range of solvents has to be solved to be used as an automated chemical synthesis equip-

ment.

Cantilever arrays coated with a range of printed sensing material have been reported[21]. A chemical gas sensor was fabricated by printing thin layers of different polymers from dilute solutions onto cantilevers. It has been demonstrated that the inkjet method is faster and more versatile than other coating methods such as microcapillaries or pipettes. Furthermore, it is capable of coating large arrays and arbitrary structures.

Printing energy storage devices is also one of the emerging research areas aiming to satisfy the growing demands for portable electronic devices that are low cost, thin, lightweight, and potentially also flexible. Especially, with the emergence of printed electronics such as RFID tags, smart cards, electronic paper, and wearable electronics, it has become increasingly important to develop printed energy storage devices[22].

A micro-supercapacitor which is integrated with a MEMS based energy harvesting device is fabricated with inkjet printing technology and described in the reference[23]. Activated carbon particles are mixed with PTFE polymer binder in ethylene glycol. Triton X-100 surfactant was added to the solution in order to increase the wettability and the stability of the emulsion. The inks were deposited onto the interdigitated gold fingers. The substrate is then heated at 140°C in order to get an homogeneous activated carbon deposition. The device was characterized

with electrochemical techniques in 1 M Et₄NBF₄ and demonstrated a wide potential range (2.5 V) with a cell capacitance of 2.1 mF/cm².

There are research reports describing electroactive polymer ink preparations that can be used with inkjet printing methods. X. Li *et al.* have demonstrated a dispersed conducting polyaniline/silica ink preparation by using hydrolysis and condensation of tetraethyl orthosilicate (TEOS)[13]. Polyaniline (PANI) is a conducting polymer which has received significant attention due to its good stability and interesting redox response [14]. P. Gajendran and R. Saraswathi [24] have reported PANI-CNT (Carbon Nanotube) composite inks. PANI-CNT composites are dispersed in aqueous solution in spite of the insoluble nature of PANI in water. A 1:3 nitric acid - sulfuric acid treatment converted the hydrophobic property of CNTs to hydrophilic due to the incorporation of acid functionalities and allowed the PANI-CNT composites to be dispersed in aqueous solutions.

With motivations of increasing demands for the printable energy storage devices, an all printed flexible PEDOT:PSS supercapacitor is fabricated and characterized as a prototype device in this thesis.

2.2 Characterization of the printing parameters

There has been considerable research investigating the relationship between droplet formation and control parameters. Droplet formation of silver nanoparticles (around

4 nm) is investigated by M. H. Tsai *et al.* [25]. It is generally accepted that droplet size is determined by the radius of the nozzle orifice. However, an order of magnitude reduction in drop volume with same nozzle has been demonstrated by adjusting the driving voltage wave form [26]. In this thesis, however, due to the relatively large size of the pattern (12 mm × 12 mm) and the ease and reliability of drop formation using PEDOT:PSS solution, we do not perform detailed investigation into these characteristics. Here, we focus on the adjustable range of printing parameters (voltage, pulse length, frequency) that result in the most uniform electrode pattern.

Higher voltage causes larger displacement of the piezoelectric actuator and thus results in higher pressure inside the nozzle. This results in increased droplet acceleration and it enables the nozzle to eject higher viscosity inks. The voltage range of the Microdrop system is 30 - 255 V. However, we observe that a voltage range of 50 - 80 V is sufficient for printing the PEDOT:PSS solution.

The voltage pulse length can be adjusted between 8 and 200 μsec . The pulse length can change droplet shape and velocity. However, it is not as critical when compared to voltage or frequency in order to get a good pattern. It is noticed that optimal droplets are achieved between 20 and 40 μsec from the experiments.

The adjustable droplet frequency range is from 1 to 3000 Hz. The fastest dispensing frequency is dependent on the properties of the liquid. Characterizing

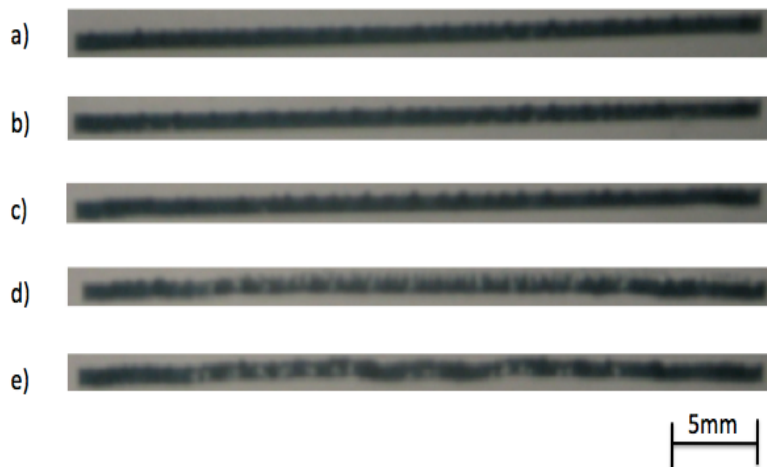


Figure 2.1: Dispensing frequency and continuous line patterning a) 333 Hz b) 833 Hz c) 1666 Hz d) 2333 Hz e) 3000 Hz.

dispensing speed is important in order to minimize electrode fabrication time. As shown in Figure 2.1, slower dispensing frequency gives better line patterning and from 2333 Hz, the printed lines are no longer uniform. For the PEDOT:PSS solution, 1666 Hz dispensing frequency which corresponds to $30 \mu\text{m}$ droplet distance and 50 mm/s stage speed is used to pattern the electrode.

2.3 Equipment setup and electrode printing

Figure 2.2 shows the experimental setup used to print the electrode. In addition to the nozzle housing, we have designed a substrate heater (right bottom of Figure 2.2). Water in the PEDOT:PSS solution causes the paper to warp during the deposition and curing process (100°C 10 minutes). The paper is placed on the substrate

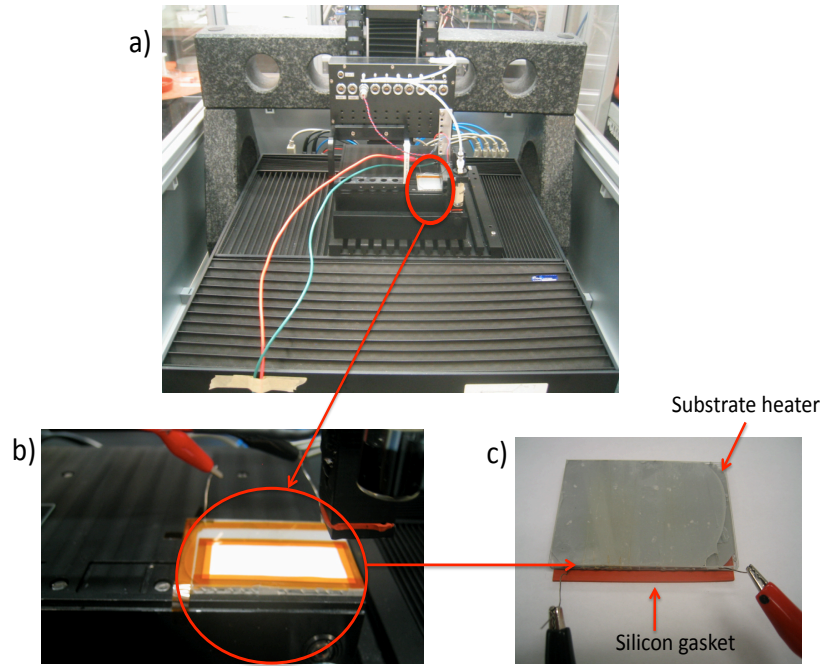


Figure 2.2: a) The inkjet printer stage setup b) the paper attachment on the substrate heater c) the substrate heater and the silicon gasket.

heater (100°C is maintained) and kapton tape is used to hold the position of both paper and substrate heater. Rapid water evaporation using this setup allows us to fabricate thick and uniform electrodes without warping commercial paper.

The substrate heater is fabricated using three glass slides, nickel-chromium alloy wire (80 % Nickel, 20 % Chromium), and thermally conductive epoxy adhesive resin. The glass slide is wrapped uniformly with the nickel-chromium wire

and an epoxy resin is applied to both sides. The glass slide is sandwiched with two additional glass slides and kapton tape is used to hold the assembly. The epoxy was cured using a hot plate (80°C, for an hour). A silicon gasket (operating temperature 204 - 260°C) is placed under the heater to reduce heat transfer to the printer stage. The temperature of the glass surface is maintained around 100°C by applying a 1.6 A current to the nickel-chromium wire.

The macro function of the inkjet printing system is used to print the electrode pattern. The macro dispensing feature enables us to control the pattern start position, size of the pattern, droplets distance, etc. Micro patterning using the microdrop printing system can be done with a repetition accuracy of $\pm 1 \mu\text{m}$ (x and y axis) and $\pm 5 \mu\text{m}$ z-axis. The PEDOT:PSS conducting polymer is deposited on both sides of the paper in order to complete the supercapacitor. Six layers are deposited to minimize electrical resistance. Considering the sensitive nature of the droplet, the droplet is checked using the strobe station after each layer is deposited. Four different commercial papers are tested as a supercapacitor substrate as shown in Figure 2.3-2.4. Due to the different chemical additives of each commercial letter size paper (from Husky xerocopy (Canada), Hansol paper (Korea), and Korea paper (Korea) for #1-1, #2-1, and #3-1), each sample shows different patterning properties such as PEDOT:PSS particle agglomeration, penetration. We choose the paper (from Neenah paper, whitestone) that is electrically insulating between the two sides and has a uniform PEDOT:PSS pattern on each side. Figure 2.4 shows the electrode patterned on the paper.

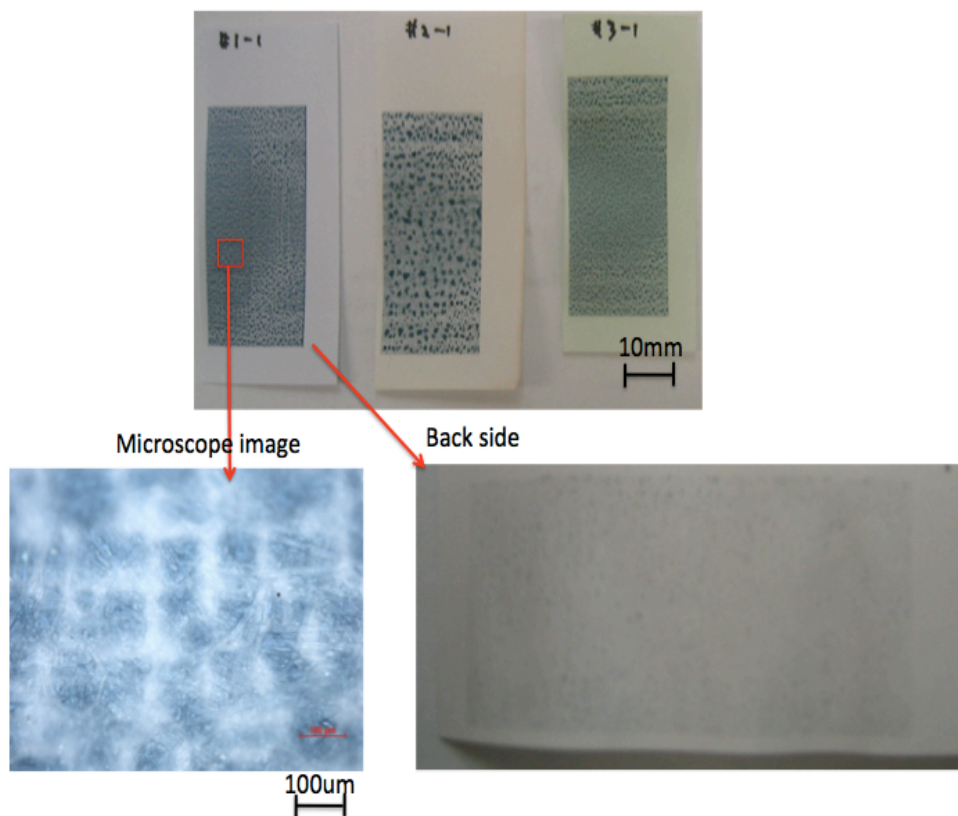


Figure 2.3: PEDOT:PSS deposition on commercially available letter size papers which are showing different particle agglomeration and penetration. #1-1, #2-1, and #3-1 are from Husky xerocopy (Canada), Hansol paper (Korea), and Korea paper (Korea), respectively.

In this chapter, the advantages and limitations of the inkjet micropatterning technology are described in various applications. With the recent research reports of droplet formation and control parameters, all the parameters (voltage, pulse length and frequency) determining droplet formation of our system are discussed. Electroanalytical experiments including cyclic voltammetry, ionic conductivity,

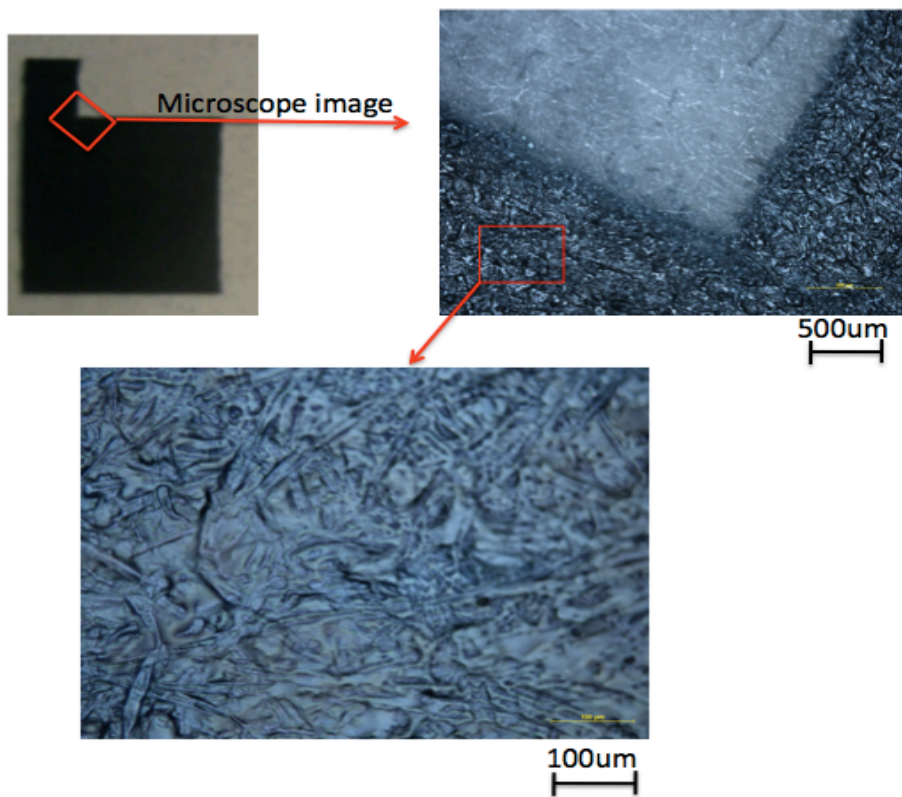


Figure 2.4: Electrode pattern on a commercial paper (whitestone, Neenah paper company, USA).

electrochemical impedance measurement will be performed with the printed PE-DOT:PSS electrode in the next chapter.

Chapter 3

Experiments and results

In this chapter, the capacitance of the printed supercapacitor is measured and the origin of the capacitance is explored. It is also suggested that porosity can be increased by using the surfactant Triton X-100. In Section 3.1, we discuss experimental results and limitations of using atomic force microscopy (AFM), field emission scanning electron microscope (FESEM), and the BET (Brunauer, Emmett, and Teller) techniques to characterize the porosity of the PEDOT:PSS electrode. Ionic conductivity measurement of the PEDOT:PSS film using a custom made apparatus are introduced in Section 3.2. A decrease in the ionic resistance of the sample with Triton X-100 suggests that the addition of Triton X-100 leads to increased porosity. In Section 3.3, electrode porosity is further investigated using the capacitor charge/discharge response. Varying scan rates (10 mV/s, 1 mV/s, and 0.1 mV/s) are applied to study the relationship between increased capacitance and the addition of Triton X-100. The electrochemical impedance spectroscopy

(EIS) measurements are detailed in Section 3.4 as a means to understand the factors that affect the charging rates. EIS response is compared to the result of cyclic voltammetry (CV) experiments in order to relate the frequency response to the time domain response. A trend of increased capacitance at low frequencies and long times is found in the measurements.

3.1 Porosity measurements with AFM, FESEM, and BET technique

Initially, Triton X-100 ($C_{14}H_{22}O(C_2H_4O)_n$), which has a hydrophilic polyethylene oxide group and a hydrophobic hydrocarbon lipophilic group, is added to increase hydrophilicity of aqueous PEDOT:PSS solution in order to enhance the adhesion to the paper substrate. However, in addition to the increased adhesion, it was also found to increase the capacitance of the electrode at high scan rates as shown in Table 3.1.

Table 3.1: Volume capacitance decreases as scan rate increases, WT and NT refer to electrodes with Triton X-100 and without Triton X-100 respectively.

Sample	Scan rate(mV/s)	Volume capacitance(F/cm^3)	Increase(%)
WT/NT	10	3.01/1.56	93
WT/NT	1	5.98/4.09	46
WT/NT	0.1	9.36/9.09	3

There are research reports that suggest the addition of Triton X-100 increases

the porosity of polymer electrodes and yields a higher specific capacitances[27][28]. To date, there are no reports demonstrating that addition of Triton X-100 increases the porosity of the PEDOT:PSS electrode. In order to investigate the effect of Triton X-100 on the PEDOT:PSS electrode, we add 0.3 wt% Triton X-100 with 94.7 wt% PEDOT:PSS solution and 5 wt% Ethylene Glycol and refer to this sample as WT (with Triton X-100). For the NT (without Triton X-100) sample, we only use 95 wt% PEDOT:PSS solution and 5 wt% Ethylene Glycol.

The surface morphology of two WT and NT samples were been measured with atomic force microscopy (AFM) as shown in Figure 3.1. WT (160.752 nm) shows higher standard deviation than NT (44.699 nm), which suggests that the addition of Triton X-100 increases surface roughness. It has been found that this approach has limitations. The surface roughness of the electrode could not provide the whole porosity property of the PEDOT:PSS electrode even though we can see the effect of the Triton X-100 on the surface morphology.

Cross sectional images were taken in order to characterize the porosity of the electrode. Figure 3.2 shows the cross section image of the PEDOT:PSS electrode measured by field emission scanning electron microscope (FESEM). We found that the images do not reveal the porosity directly because we need to see both sides of same fractured spot in order to determine whether or not the pore shape structure came from the fracture process or it is pristine pores.

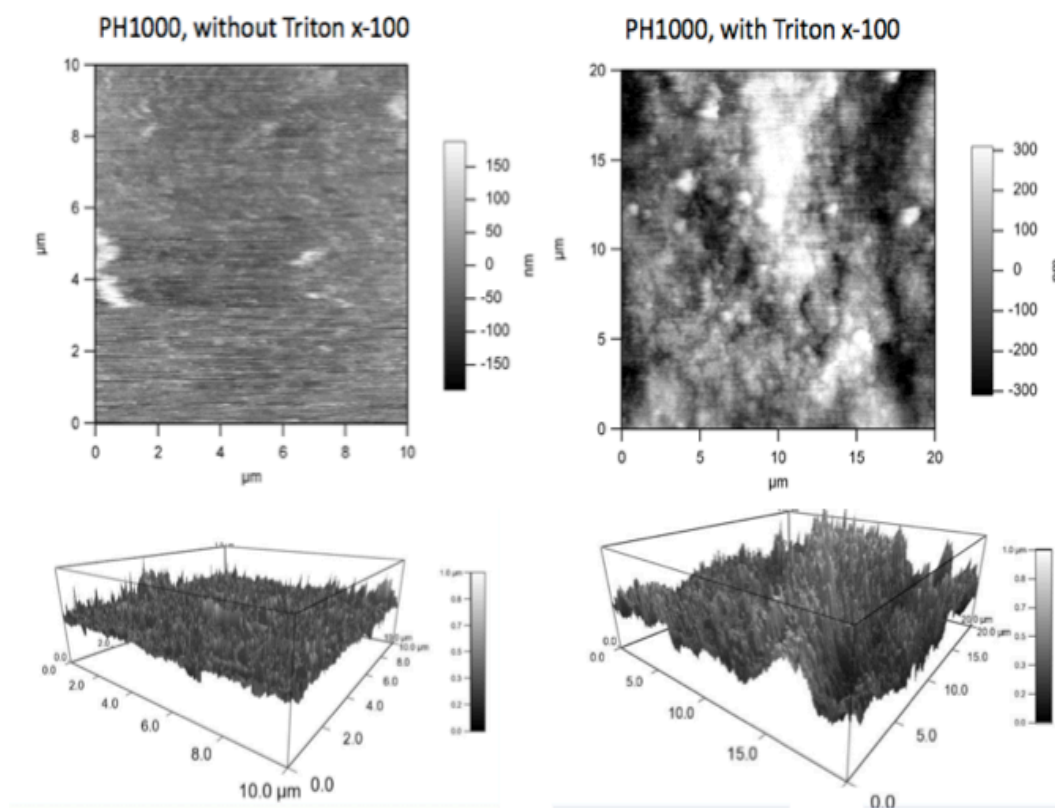


Figure 3.1: AFM images for both WT and NT samples.

The BET (Brunauer, Emmett, and Teller) measurement was also taken to characterize the surface area. However, it has been found that there is no measurable surface area with the N_2 gas adsorption BET test[29]. It seems likely that the structure of the PEDOT:PSS is sufficiently dense so that there is no significant insertion of nitrogen, and that any increase in porosity is at the molecular scale.

In the next subsection, we will perform ionic conductivity measurements to

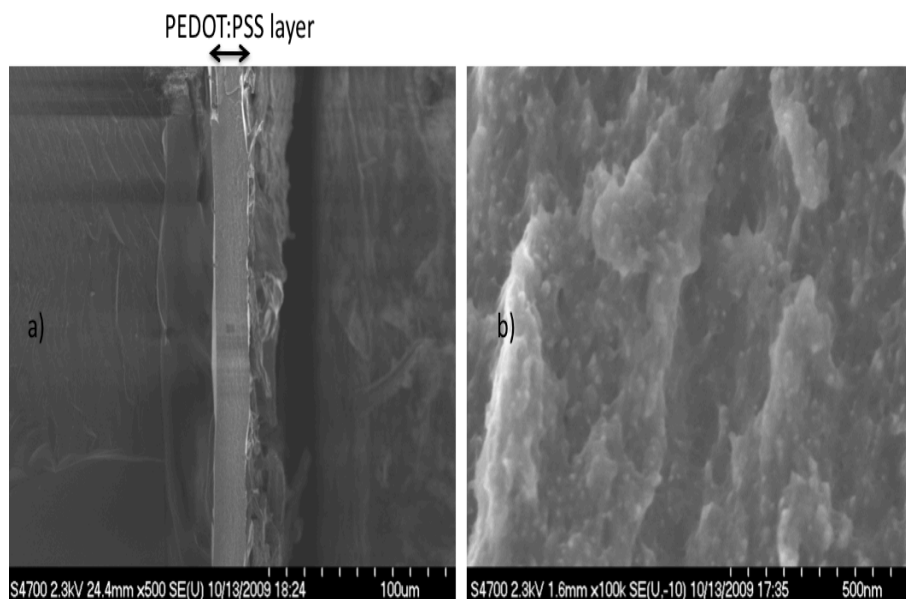


Figure 3.2: Cross section images of the electrode from FESEM.

demonstrate that addition of Triton X-100 increases ion transport rates in PEDOT:PSS electrodes.

3.2 Ionic conductivity

In the equivalent circuit of the electrode, an ion conductive pathway is represented by an ionic resistance (R_i) which is related to the porosity of the electrode. For instance, higher porosity electrodes will demonstrate lower resistances and more dense electrodes will show higher resistances. Thus the R_i of PEDOT:PSS electrode is measured to investigate the porosity effect of Triton X-100.

A custom made ionic conductivity test apparatus is used as shown in Figure 3.3. The distance between two reference electrodes is designed to be 5.2 mm by using curved tips inside the glass apparatus and the diameter of the joint part is 10 mm. The sample is sandwiched between two electrolyte reservoirs and the position is fixed by using a spring clamp.

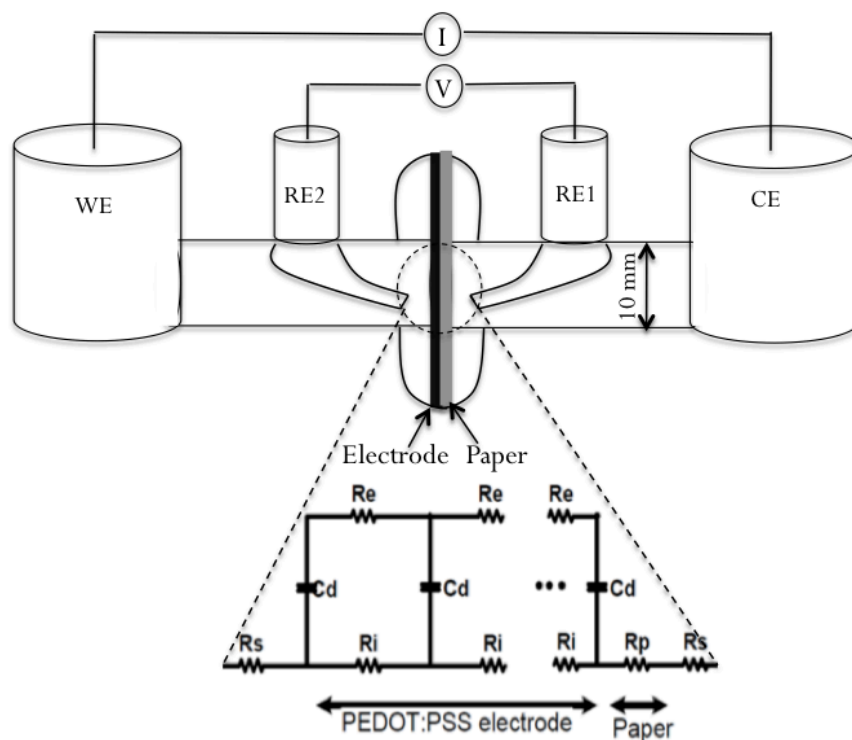


Figure 3.3: Ionic conductivity test apparatus and the equivalent circuit of the ionic conductivity measurement. WE, RE, and CE refer to working electrode, reference electrode, and counter electrode respectively. The sample is placed at the center, clamped between two circular cups.

The equivalent circuit of ionic conductivity measurement is shown in Figure

3.3. R_s , R_i , R_e , and C_d are solution resistance of the electrolyte reservoirs, ionic resistance of the sample, electrical resistance of the sample, and internal double layer capacitance respectively. R_i , R_e , and C_d of PEDOT:PSS electrode are connected in series with the paper resistance (R_p). Both ends of the electrode and paper are facing the electrolyte (0.1 M TBAP propylene carbonate), which is represented as R_s .

At high frequency, C_d becomes a short circuit and R_i is much higher than R_e so the impedance approaches the sum of R_s , R_e , and R_p . At low frequency, the impedance approaches the sum of R_s , R_i , and R_p because C_d acts as an open circuit. A separate test is performed to measure R_s and R_p of the bare paper. The ionic resistance of the electrode is calculated by subtracting R_s and R_p values from the total resistance at low frequency.

It has been noticed that the resistance of the paper (R_p) decreases over time and saturates to approximately 840 Ω after soaking in the electrolyte for six hours. As a result, all samples were soaked for more than six hours in electrolyte prior to the measurement.

Ionic resistance (R_i) has the relationship with the ionic conductivity (σ_i) as,

$$R_i = \frac{T}{\sigma_i \times \pi \cdot r^2}, \quad (3.1)$$

where T is the thickness of the electrode and r is the inner radius of the apparatus. By using above equation, ionic conductivities of WT (2.57×10^{-4} (S/m)) and NT electrode (1.04×10^{-4} (S/m)) are calculated.

From the ionic conductivity test result, it appears that the addition of Triton X-100 increases the porosity of the PEDOT:PSS electrode. In the next subsection, it will be shown how this change of R_i affects capacitor charge/discharge response.

3.3 Cyclic voltammetry

Cyclic voltammetry (CV) is one of the most widely used electroanalytical techniques used to study electrochemical systems in the time domain. During a CV experiment, a potential sweep of constant rate (voltage/second) is applied to the working electrode (WE) with respect to the reference electrode (RE). The current that flows from the working electrode to the counter electrode (CE) is measured to determine the overall electrochemical response. When the CV reaches a set potential, the potential sweep is reversed. This cycle is typically repeated and the data is plotted as current (i) vs. potential (E).

The basic relationship between stored charge (Q) to capacitance (C) at a given voltage (V), is given as

$$Q = C \cdot V, \quad (3.2)$$

and the current,

$$I = \frac{dQ}{dt} = C \cdot \frac{dV}{dt}. \quad (3.3)$$

Recognizing that dV/dt is potential scan rate v , we get,

$$C = \frac{I}{v}. \quad (3.4)$$

With this simple derivation, we get an expression for the capacitance as a function of current at a given scan rate.

Cyclic voltammetry measurements are performed using a Solatron 1287A Potentiostat/Galvanostat with a three electrode system, which is composed of working electrode (WE), reference electrode (RE), and counter electrode (CE). Propylene carbonate electrolyte with 0.1 M tetrabutylammonium perchlorate (TBAP) and Ag/Ag⁺ ion reference electrode (0.1 M TBAP, 0.01 M AgNO₃), and active carbon (carbon-filled polytetrafluoroethylene, from W. L. Gore & Associates) counter electrode are used for these tests.

The volume capacitance of both the WT and NT electrodes is measured at several scan rates to investigate the effects of porosity for capacitor charge/discharge. It has already been reported[30]-[32] that lower scan rate can yield higher capacitance. When the electrochemical double layer capacitors are charged, the rate is limited by the RC charging times. At a high scan rates, only part of the electrode

is charged, whereas ions can have more time to penetrate deep inside the electrode at a lower scan rate. Thus we measure higher volume capacitance at lower scan rates.

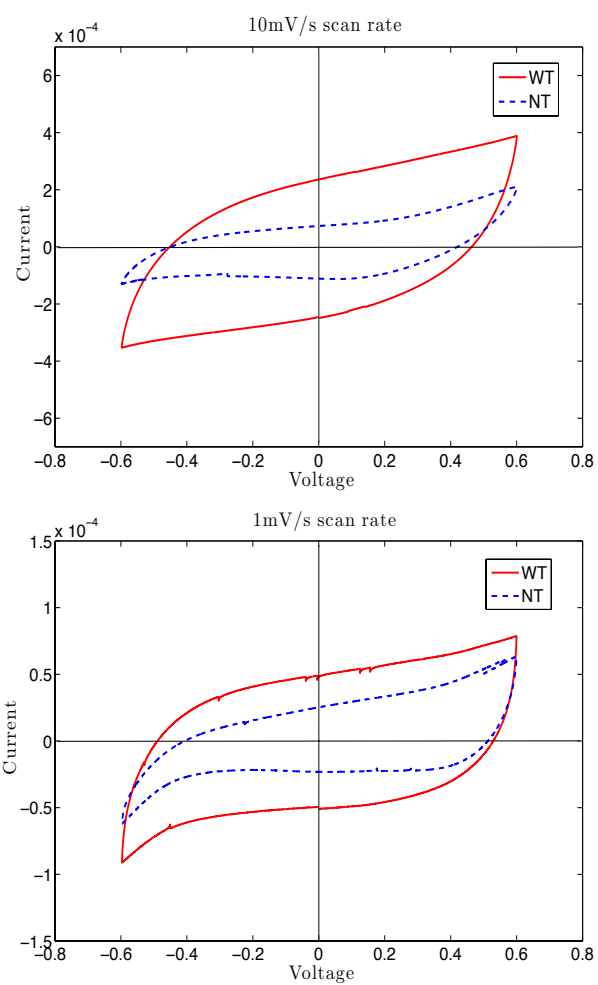


Figure 3.4: The cyclic voltammetry of the PEDOT:PSS electrodes at 10 mV/s (top) and 1 mV/s (bottom) scan rates.

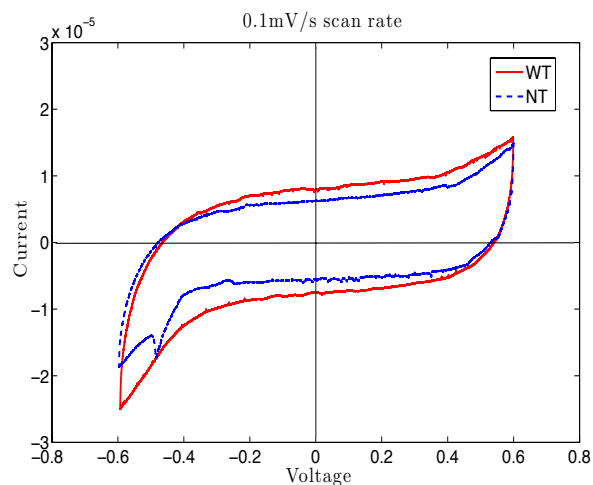


Figure 3.5: The cyclic voltammetry of the PEDOT:PSS electrodes at 0.1 mV/s scan rate.

As summarized in Table 3.1, both WT and NT electrodes show increased capacitance at lower scan rate. The WT electrode demonstrates higher volumetric capacitance than NT electrode, particularly at intermediate and fast scan rates. This can be explained with the reduced time constant of WT electrode due to the increased porosity. However this volume capacitance difference is not apparent at 0.1 mV/s (3 %). This suggests that Triton X-100 can improve the charge/discharge speed but it does not increase the capacitance itself.

Cyclic voltammetry measurements for both WT and NT at different scan rates (10 mV/s, 1 mV/s, 0.1 mV/s) are presented in Figures 3.4-3.5. The CV plot shows a deviation from the ideal rectangular shape. In particular the CV plots of 10 mV/s scan rate shows a slope throughout the charge/discharge cycle, and therefore

a slow increase in the capacitance. If the time constant for electrode charging is lower than the complete scan time, capacitance can increase throughout the charge/discharge cycle. From equation (3.4), we can see that current is function of the capacitance. The CVs show sharp increase in the current at both ends of the voltage window at lower scan rates. This can be explained by the charge transfer reaction that is a function of the applied potential to the electrode. Equation (3.3), shows that reduced electrode current can make the reaction currents more apparent at slow scan rate

3.4 Electrochemical impedance spectroscopy

Electrochemical impedance spectroscopy (EIS, sometimes also called AC impedance) is a powerful diagnostic tool in the analysis of electrochemical systems. By measuring the impedance of a system over range of frequencies, we can characterize the energy storage behavior and utilize this information to improve the performance of the system.

A low AC perturbation potential is applied to the cell in order to charge/discharge the electrode. Ion movement associated with the energy storage elements will induce an AC which flows through the cell. Electrochemical impedance is calculated as the rate of the applied potential and measured current into the device. A frequency response analyzer (FRA) is used to measure the phase shift which can determine whether the cell response is capacitive, inductive, or resistive at a particular frequency.

In the equivalent circuit analysis, the ionic resistance represents an ionic conductive path through an electrode and a capacitor forms the energy storage element. With the AC potential input, the resulting output current signal is at the same frequency but is shifted in phase and has different amplitude. The phase provides information on the nature of the device impedance. For instance, with zero phase, the system is behaving in a purely resistive manner. For 45° phase, ions diffuse inside but have not reached the end of the electrode[33]. For 90° phase, it responds purely in a capacitive manner. The magnitude ratio between input voltage and output current, along with phase, can be used to evaluate both the real and imaginary impedance at any frequency.

The measured EIS impedance and phase information is expressed graphically with Bode plots, which depict the magnitude and phase of the impedance as a function of frequency, or with the Nyquist plots on which the real and imaginary parts of impedance are plotted.

The three electrode cell setup, with a Solatron 1287A Potentiostat/Galvanostat, 1260A Impedance/Gain-phase Analyzer, is used for the EIS experiments. It is noticed that direct electrical connection to the electrode using an alligator clip induces corrosion to the alligator clip due to reactions with the paper substrate soaked with electrolyte. In order to avoid the corrosion, aluminum foil is attached on top of the paper using kapton tape. The paper is cut in half through the thick-

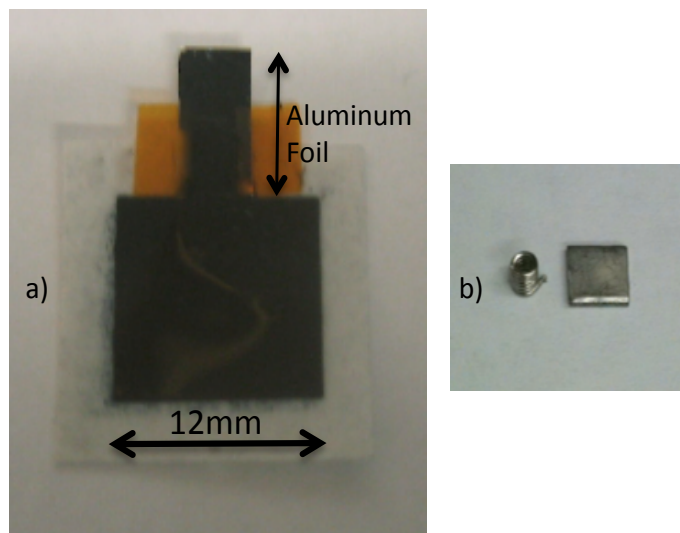


Figure 3.6: a) Electrode with aluminum foil substrate b) coil shape platinum wire and stainless steel sheet piece.

ness in order to minimize the gap between the paper and the aluminum foil. As shown in Figure 3.6 the PEDOT:PSS electrode is deposited on both paper and aluminum foil without electrical disconnection. After curing the electrode, electrical resistance is measured to ensure the solid electrical contact between aluminum foil part electrode and the main rectangular electrode. Coiled platinum wire (top) and rectangular stainless steel sheet (bottom) are used to connect the alligator clip to the electrodes in order to prevent corrosion between the alligator clip and the electrode.

A stainless steel wire of 0.7 mm diameter is connected in parallel to the refer-

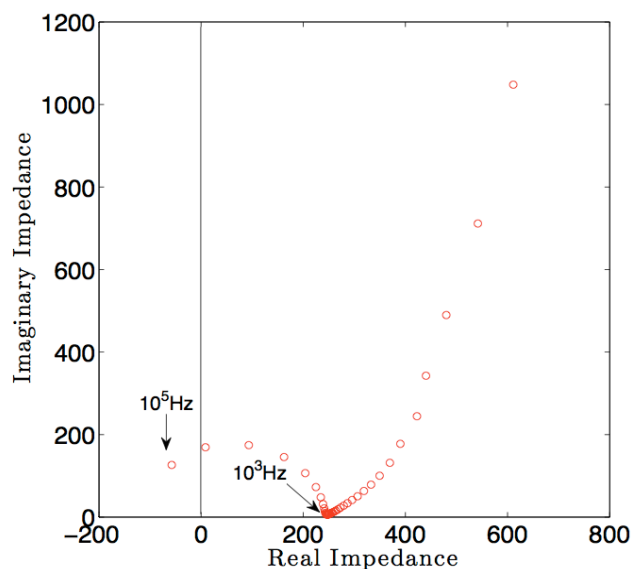


Figure 3.7: Abnormal impedance response without stainless steel wire connection to RE at high frequency.

ence electrode (RE) to remove the high frequency abnormal response. Figure 3.7 shows there is an unexpected impedance response from 10^5 Hz to 10^3 Hz. We believe the RC delay caused by RC components inside reference electrode induces this phenomenon at high frequency. Thus a stainless steel wire is connected in parallel to the RE to make another repeatable ground path at high frequency. In order to see the input capacitance effect, $0.1 \mu\text{F}$, $2.2 \mu\text{F}$, $4.7 \mu\text{F}$ capacitance are connected in series with the stainless steel wire. However, it was found that all capacitance values corrected the high frequency response and as a result, only the stainless steel wire is connected as shown in Figure 3.8.

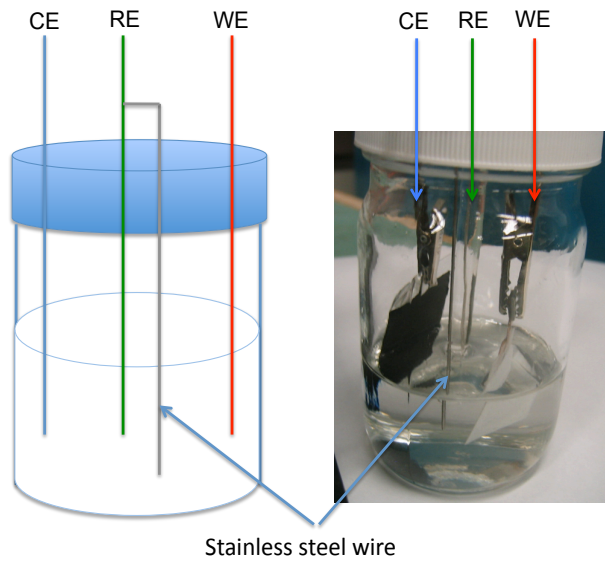


Figure 3.8: The EIS three electrode cell setup.

From 10^5 Hz to 10^{-4} Hz, 0 V DC, 50 mV AC input setup is used for the test. A 50 mV AC input is found to give good signal to noise while not including a non-linear response. A 50 mV AC input measurement data is compared with 10 mV AC input response to ensure it is tested in the linear response regime.

From the phase angles (45° , 67.5° , and 90°) of the Bode plot, the capacitor charge condition can be inferred. A phase angle of 45° can be associated with the fact that the ions do not reach the end of the electrode[33] and therefore it is called as an infinite response. The 90° phase angle suggests that the electrode behaves purely capacitive manner. The phase angle 67.5° is transition angle from infinite

diffusion response to capacitive response, which corresponds to the RC time constant. The RC time constant of the WT electrode is 50.46 s (3.15×10^{-3} Hz) and of the NT electrode is 112.9 s (1.41×10^{-3} Hz) that is demonstrating the effect of addition of the Triton X-100.

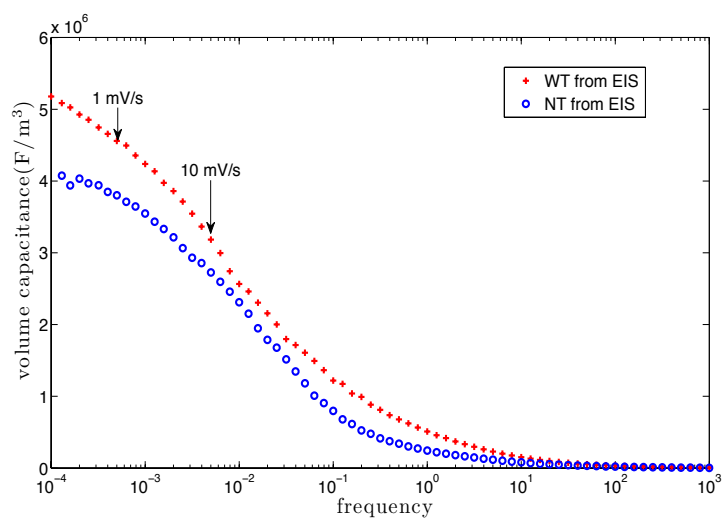


Figure 3.9: Volumetric capacitance vs. frequency plot from the EIS and its corresponding scan rate in the CV.

It was previously mentioned that the scan rate does affect the observed capacitance in the CV measurement. We calculated a volume capacitance (F/m^3) from the EIS measurement in order to see whether we can observe same response in EIS. Imaginary impedance of the EIS is used to calculate the capacitance by using the capacitance and impedance relationship,

$$Z = \frac{1}{j\omega \cdot C}. \quad (3.5)$$

The volume capacitance is plotted as a function of frequency and two scan rates (10 mV/s and 1 mV/s) are noted in Figure 3.9. In order to calculate the frequency which corresponds to each scan rate, the relationship given as

$$f = \frac{1}{2 \cdot \pi \cdot \tau}, \quad (3.6)$$

is used, where f is the frequency and τ is the RC time constant which is calculated from cyclic voltammetry experiment at each scan rate.

The volume capacitance calculated from the equation (3.6) is summarized in Table 3.2. The scan rate 0.1 mV/s (6.12×10^{-5} Hz) is out of the EIS test frequency range thus it is not compared.

Table 3.2: Volume capacitances calculated from the EIS data for both WT and NT at different scan rates.

Sample	Scan rate(mV/s)	Volume capacitance(F/cm ³)	Increase(%)
WT/NT	10	3.18/2.72	19
WT/NT	1	4.56/3.84	17

Unlike results of the CV test (Table 3.1), the capacitance ratio decreases between the WT and NT at lower scan rates are not obvious in the EIS measurement. The voltage range and the signal difference might cause this differences. The voltage range of the CV is ± 0.6 V which is in non-linear impedance response range,

whereas it is linear regime ($\pm 50\text{mV}$) in the EIS. The voltage input for the CV is linearly increasing, whereas the EIS input is the sinusoidal.

In this chapter, we have shown that the charging rate of the PEDOT:PSS electrode is increased by using the surfactant Triton x-100. With the CV measurement, it has been found that the WT electrode demonstrates higher volumetric capacitance than NT electrode at intermediate and fast scan rates. An attempt has been made to relate the time domain response (CV) to the frequency domain response (EIS). However, the capacitance ratio decrease between the WT and NT at lower scan rate is not obvious in the EIS measurement.

Chapter 4

Multiple time constant model

In Chapter 3, electroanalytical measurement techniques are utilized in order to characterize the performance of the printed supercapacitor. Volume capacitances of 9.36 F/cm^3 and 9.09 F/cm^3 are measured for both the WT electrode and NT electrode. Although the magnitude of the capacitance is similar, different charging times are observed, e.g., 50.46 s for the WT electrode and 112.9 s for the NT electrode. In order to investigate the rate limiting factors of capacitor charging, an equivalent circuit model is utilized. A multiple time constant model is proposed in order to explain physical origin of the distributed time constant behaviour. The thickness variation of the PEDOT:PSS electrode is assumed to be the primary reason of the measured behavior and thus actual thickness variation is incorporated in the modelling. The CPE response and its physical origin are discussed in Section 4.1. The origin of capacitance distribution of the PEDOT:PSS electrode is described in Section 4.2. In Section 4.3, a multiple time constant model is con-

structured based on thickness variation of the electrode. Data fitting with the EIS experiment of the WT electrode suggests that thickness variation is not the only factor leading to increase in capacitance distribution. Finally, in Section 4.4, all the parameters used in modelling are compared to the experimental data.

4.1 The origin of the CPE response

A frequency dispersive response is often observed in EIS and cannot be explained by simple arrangements of passive electrical elements such as resistors, capacitors, or inductors. A common form of the response observed in electrochemical systems, but for which concrete physical explanations are usually lacking, is the constant phase element (CPE) impedance given by

$$Z(\omega) = \left(\frac{1}{C_{CPE}} \right) (j\omega)^{-\alpha}, \quad (4.1)$$

where C_{CPE} and α are the CPE coefficient and the CPE exponent respectively.

The time constant dispersion mainly caused by the capacitance dispersion is the critical aspect necessary to explain the capacitor charge/discharge response. Thus, extensive attention has been paid to investigate the capacitance dispersive response. The CPE is widely used in electrochemical impedance modelling in order to represent time constant distribution in an equivalent circuit [34]-[35]. It

also demonstrates excellent fit to the EIS results in our experiments. However, it does not help to identify the physical origin of this behaviour.

There are research results demonstrating pore size distribution [36] or pore length distribution [37] as a physical origin of frequency dispersion. In these two reports, analytical modelling is performed to explain the abnormal EIS response of activated carbon fiber cloth electrode (ACFCE). The measured phase angle of the impedance spectrum was larger than 45° at high frequencies and smaller than 90° at low frequencies. Song *et al.* [36], explained it using a dispersed pore size distribution (PSD), whereas Lee *et al.* [37], demonstrated better fitting with a pore length distribution (PLD). They also mentioned that the PSD of the ACFCE is quite narrow and thus the PSD has a negligible influence on the non-ideal impedance behaviour of the AFCC. The PLD theory has demonstrated improved fitting and it also has a clear physical basis. However, their approach was restricted to cylindrically porous electrodes. This is not applicable to the analysis of nanoparticle composite electrodes used in this study.

Transmission line models of micro-to-nanoporous activated carbon materials composed of agglomerates and grains have been reported [38]. Linear transmission lines and self-affinity fractal geometry were used to create an equivalent circuit model. In general, they demonstrated a successful impedance response model with different electrode conditions such as electrode thickness, agglomerate radius, and pore size distribution. It has been demonstrated that size of the

agglomerated particle affects the capacitance and charging property; i.e., large interfacial area with small ion transport paths of small particles show higher capacitance but slow charge/discharge time compared to large particles. However, faradaic impedance was not taken into account in the modelling.



Figure 4.1: Microscope image of the PEDOT:PSS electrode surface.

It has been noted that the specific capacitance per unit area of the carbon electrode ranges from about $1 \mu\text{F}/\text{cm}^2$ for the basal plane to $70 \mu\text{F}/\text{cm}^2$ for the edge plane [39]. It has been demonstrated experimentally that the CPE exponent α decreases with increasing amount of the edge orientation of the carbon electrode. This result suggests that increased distribution of capacitance induced by inhomogeneity of the surface causes frequency dispersive response. Z. Kerner and T. Pajkossy have reported that atomic scale inhomogeneities of the electrode are

the reason of capacitance dispersion and experimentally demonstrated its effect in CPE response [40].

4.2 The origin of capacitance distribution of the PEDOT:PSS electrode

The capacitance distribution of the PEDOT:PSS electrode is also believed to be the physical origin of the CPE response. The likely factors which can cause the capacitance distribution are investigated in this chapter. As mentioned in fabrication section, aqueous PEDOT:PSS solution which consists of 30 - 100 nm particles [41] is deposited on commercial paper by an inkjet printing process as shown in Figure 4.1. During the deposition, the sample is cured by a substrate heater (100 °C) to evaporate water solvent quickly. This curing condition may enhance the hydrodynamic flow inside the deposited solution [42] and it can induce inhomogeneous thickness variation.

The thickness variation measurements are performed by using the Dektak 150 surface profiler (from Veeco company, USA). PEDOT:PSS is deposited from top to bottom and thickness is measured along the five lines shown in Figure 4.2. Figure 4.3 shows that thickness profile of the WT electrode is flatter than that of the NT electrode, which is believed to be the effect of the Triton X-100.

It is observed through the experiment that a curing temperature of around

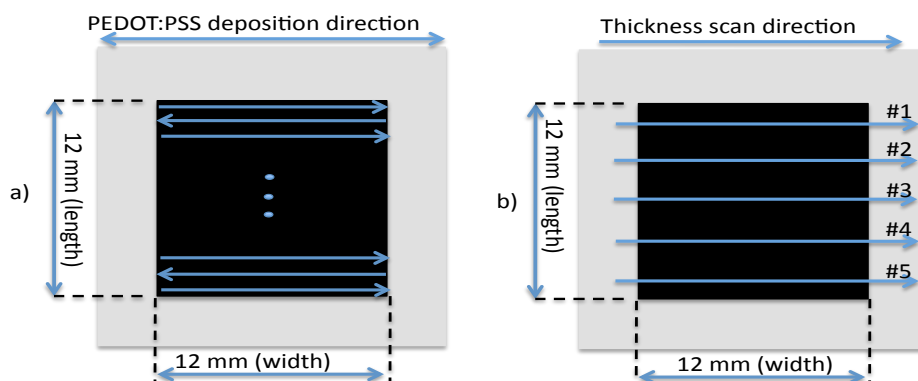


Figure 4.2: a) The deposition direction (from top lines to bottom lines) of the PEDOT:PSS electrode b) the thickness scan direction of the PEDOT:PSS electrode.

Table 4.1: The average thickness of the two PEDOT:PSS electrodes (WT and NT) and bare paper roughness along five different lines.

Sample	#1 (μm)	#2 (μm)	#3 (μm)	#4 (μm)	#5 (μm)
WT	16.8	10.0	43.0	37.1	33.7
NT	6.7	23.7	69.3	70.8	49.6
Bare paper	3.5	NA	3.2	NA	3.1

130°C causes the PEDOT:PSS electrode to lift off from the paper substrate or break the pattern. Therefore, the temperature of the substrate heater was maintained around 100°C. However, the temperature is not sufficiently high to get instant water evaporation due to the reduced heat transfer through the paper.

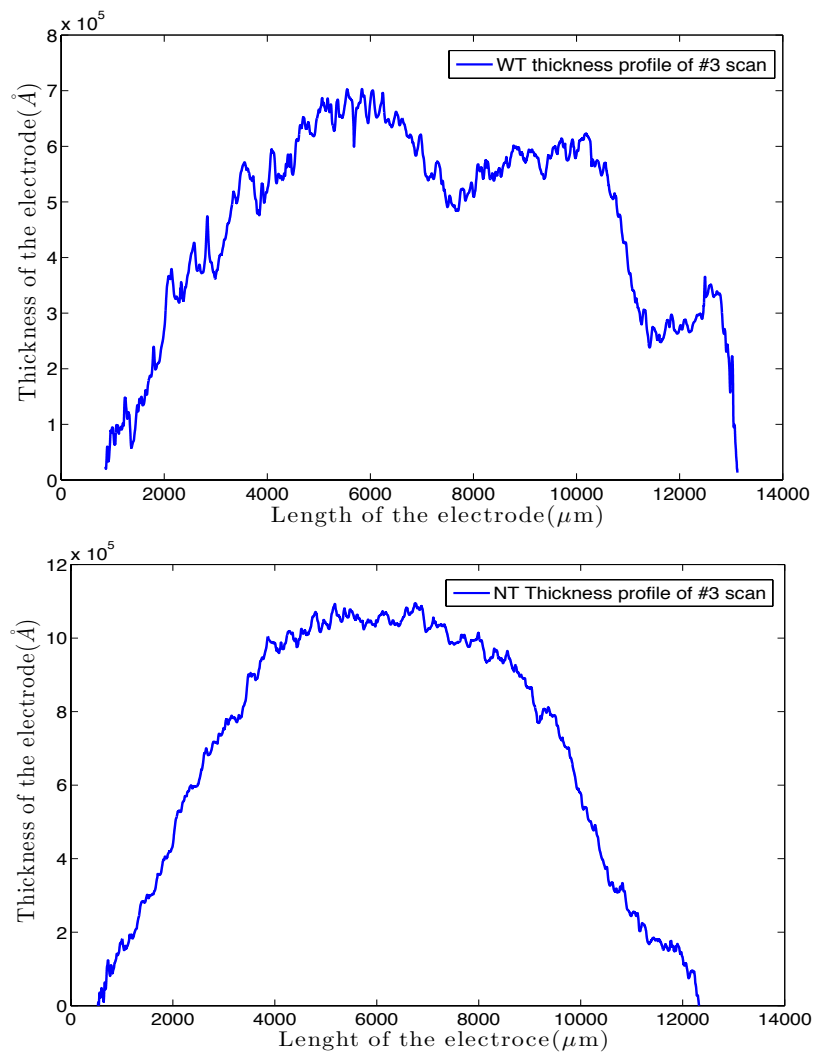


Figure 4.3: Thickness profile for both WT and NT electrodes at #3 (center) position scan.

It is observed that the parts of the PEDOT:PSS electrode along the top lines are evaporated faster than bottom lines and it took time to completely evaporate

water of the bottom of the electrode. We believe that slower evaporation time than accumulation of droplets caused asymmetric evaporation time and it caused hydrodynamic flow towards the center of the electrode from the top lines.

The thickness variation caused by nanofibers of the paper substrate is measured. However it is found to be minor (3.1 - 3.5 μm) compared to the thickness of the electrode as shown in Table 4.1. The total thickness variations of the PEDOT:PSS electrode which is measured from scan #1 to #5 are shown in Figure 4.4. The histogram suggests that the thickness variation is not following a Gaussian distribution or lognormal distribution which is often used in analytical modelling [36] - [37]. In the next chapter, the measured thickness is incorporated into a proposed model and the results are compared to the fitting that has used lognormal distribution.

4.3 Multiple time constant modelling

The transmission line model using multiple time constants has been constructed to represent the dispersed capacitance behaviour of the electrode. Based on the thickness measurement data in Figure 4.4, a transmission line model with different thickness sections is proposed. A difference in height means that at different locations it takes more or less time to charge the sample, as the time for ion transport through the thickness will vary with height. This variation is simulated by modelling each sample as 200 parallel transmission lines, with the distribution of

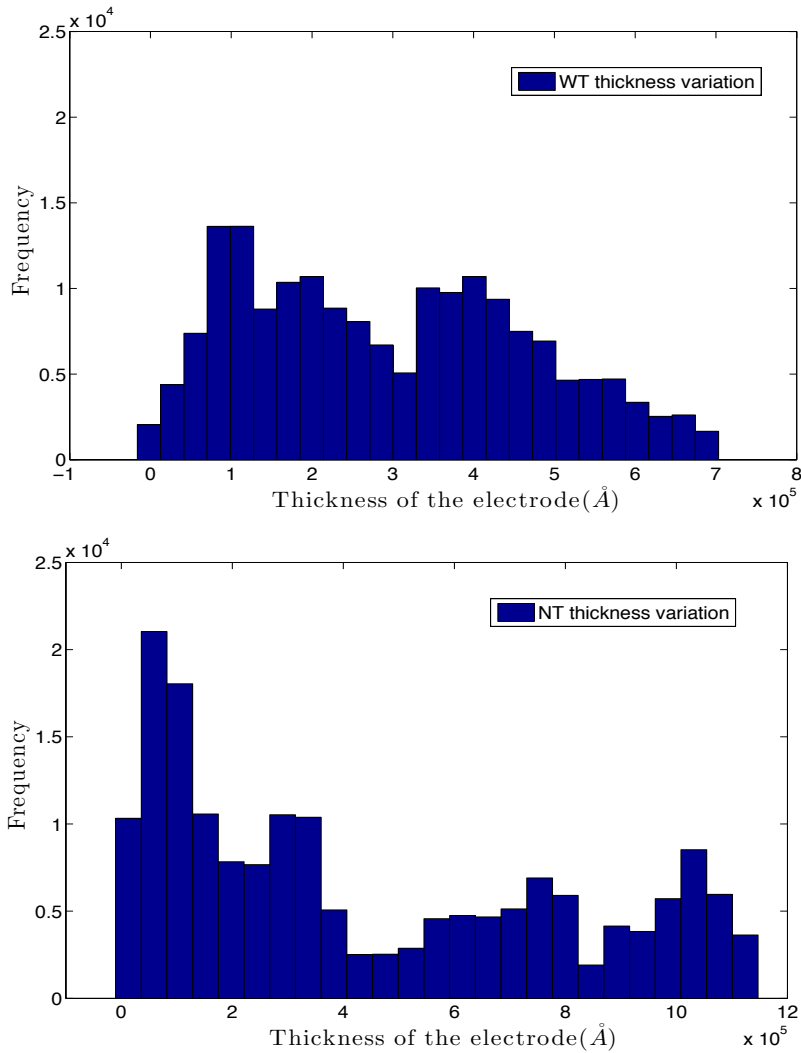


Figure 4.4: The total thickness deviation of the PEDOT:PSS electrode which is measured from scan #1 to #5.

transmission line lengths matching the measured height distribution. Using this approach, each electrode is divided into 20 x 10 sections with distributed thickness variation. As shown in Figure 4.5, each section is treated as a separate transmis-

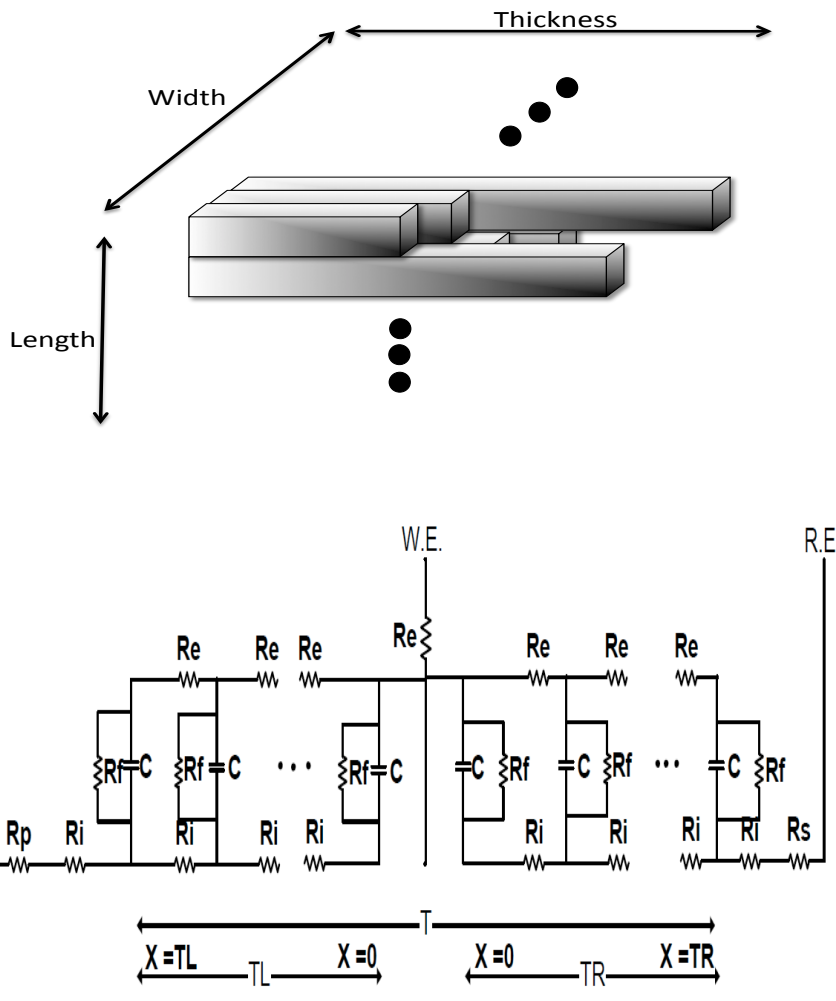


Figure 4.5: The simple drawing of the multiple thickness electrode (top) and equivalent circuit for one section of the electrode (bottom).

sion line within the multiple time constant model.

The PEDOT:PSS electrode is attached to a paper substrate and the front side

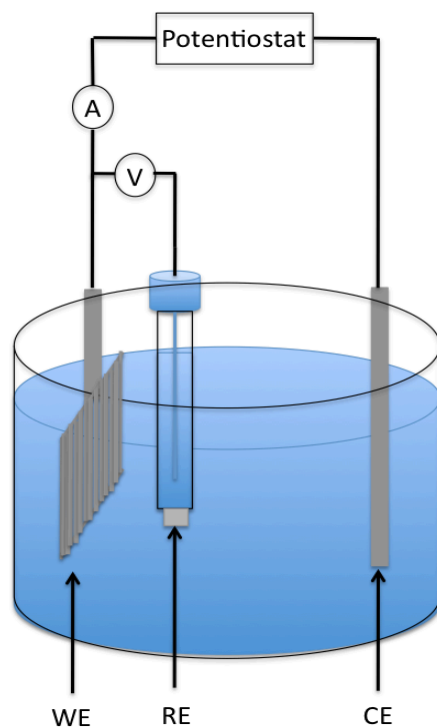


Figure 4.6: The three electrode EIS measurement setup for measuring solution resistance. A stainless steel sheet (SSS) is used as a working electrode. WE, RE, and CE refer to the working electrode, reference electrode, and counter electrode respectively.

of the electrode is facing the electrolyte phase. In the equivalent circuit in Figure 4.5, the electrical resistance, R_e , is treated as a short circuit due to its much lower resistance (about 10^3) when compared to the ionic resistance. During the electrochemical charging or discharging, ions from the electrolyte pass through a resistance of R_i and charge/discharge the capacitance. In this model, we allow the electrode to be charged from two sides, since ions enter the polymer both through the paper and from liquid electrolyte in contact with the polymer.

The front side transmission line is connected to the solution resistance, whereas back side transmission line is connected to R_p and R_s . These two transmission lines are connected in parallel to make one transmission line which represents one section of the electrode. A faradaic impedance, R_f , takes into account charge transfer reactions that are typically relevant at extremely low frequency. It is added parallel to the capacitance as shown in Figure 4.5.

In order to calculate the ion penetration depth, the solution resistance (resistance between WE and RE) is measured with three electrode measurement setup as shown in Figure 4.6. As shown in Figure 4.5, there are two solution resistances due to the PEDOT:PSS electrode charging with ions penetrated from the paper substrate. After covering one side of stainless steel sheet (SSS, 12 mm x 12 mm) completely with the kapton tape, the solution resistance, R_s , from the front side (SSS is facing RE) and back side (SSS is facing opposite direction of RE) is measured. The solution resistance between WE and RE is measured to be the same whether the stainless steel sheet is facing towards the RE or opposite direction to the RE. Therefore, the solution resistance is cancelled out when calculating RC time constant from front side charging ($R_i \cdot C_{front}$) and back side (after penetrating paper) charging ($R_i \cdot C_{back}$) in the equation below.

$$R_i \cdot C_{front} = R_i \cdot C_{back}. \quad (4.2)$$

By substituting R_i , C_{front} , and C_{back} , we have

$$R_i \left(\frac{T_R}{T} \right) \cdot C \left(\frac{T_R}{T} \right) = \left(R_p + R_i \left(\frac{T - T_R}{T} \right) \right) \cdot C \left(\frac{T - T_R}{T} \right). \quad (4.3)$$

The front side ion penetration depth is calculated as

$$T_R = \frac{R_p \cdot T + R_i \cdot T}{R_p + 2 \cdot R_i}, \quad (4.4)$$

where R_p , T_R , and T refer to paper resistance, front side ion penetration thickness, and total thickness of the electrode respectively.

Now, we derive the impedance of the right side of the RC transmission line (RCTL) in Figure 4.5. The total values of the right side of the RCTL are defined as R_{iR} (ionic resistance), C_R (capacitance), R_{fR} (faradaic resistance). We can express the voltage drop through the unit resistance R_i as

$$dV(x) = i(x) \cdot R_i \cdot dx, \quad (4.5)$$

where R_i is given by R_{iR} / T_R (Ω/cm) and T_R is the right side ion penetration thickness. We have the charging current of a unit capacitance, $di(x)$, as

$$di(x) = \frac{V(x)}{Z} \cdot dx, \quad (4.6)$$

where Z is given by $Z = R_{fR} T_R / (1 + j\omega C_R \cdot R_{fR}) (\Omega \cdot \text{cm})$. By using equation 4.5 and equation 4.6, we get

$$\frac{d^2V(x)}{dx^2} = \frac{R_i}{Z} \cdot V(x). \quad (4.7)$$

The general solution of equation 4.7 has the form

$$V(x) = A \cdot \exp\left(\sqrt{\frac{R_i}{Z}} \cdot x\right) + B \cdot \exp\left(-\sqrt{\frac{R_i}{Z}} \cdot x\right). \quad (4.8)$$

The total current is divided into unit capacitance charging currents. Near the center of the electrode (see Figure 4.5), we can define boundary condition as $x = 0$, and ionic current $i(0) = 0$, and thus we get $A=B$. The total current into the electrode must pass through the Z 's, so:

$$i(T_R) = \int_0^{T_R} \frac{V(x)}{Z} dx = \frac{A}{\sqrt{R_i \cdot Z}} \left(\exp\left(\sqrt{\frac{R_i}{Z}} \cdot T_R\right) - \exp\left(-\sqrt{\frac{R_i}{Z}} \cdot T_R\right) \right). \quad (4.9)$$

The impedance of right side of the RCTL is obtained as

$$Z_R(T_R) = \frac{V(T_R)}{i(T_R)} = \sqrt{R_i \cdot Z} \cdot \coth\left(\sqrt{\frac{R_i}{Z}} \cdot T_R\right). \quad (4.10)$$

The impedance of both sides of the RCTL which are connected in parallel in the

three electrode system is obtained as

$$Z_{RL} = \left(\frac{1}{\frac{1}{Z_{front}} + \frac{1}{Z_{back}}} \right), \quad (4.11)$$

where,

$$Z_{front} = \sqrt{R_i \cdot Z} \cdot \coth \left(\sqrt{\frac{R_i}{Z}} \cdot T_R \right) + R_s, \quad (4.12)$$

and

$$Z_{back} = \sqrt{R_i \cdot Z} \cdot \coth \left(\sqrt{\frac{R_i}{Z}} \cdot T_L \right) + R_p + R_s. \quad (4.13)$$

The total impedance of 20 x 10 RCTLs is obtained as

$$Z_t = \frac{1}{\sum_{j=1}^{20} \sum_{i=1}^{10} \left(\frac{1}{Z_{RL:i:j}} \right)}. \quad (4.14)$$

4.4 Data fitting of the multiple time constant model

The multiple time constant modelling proposed in Section 4.3 is compared to the EIS experimental result in this section. In order to fit the experimental data, capac-

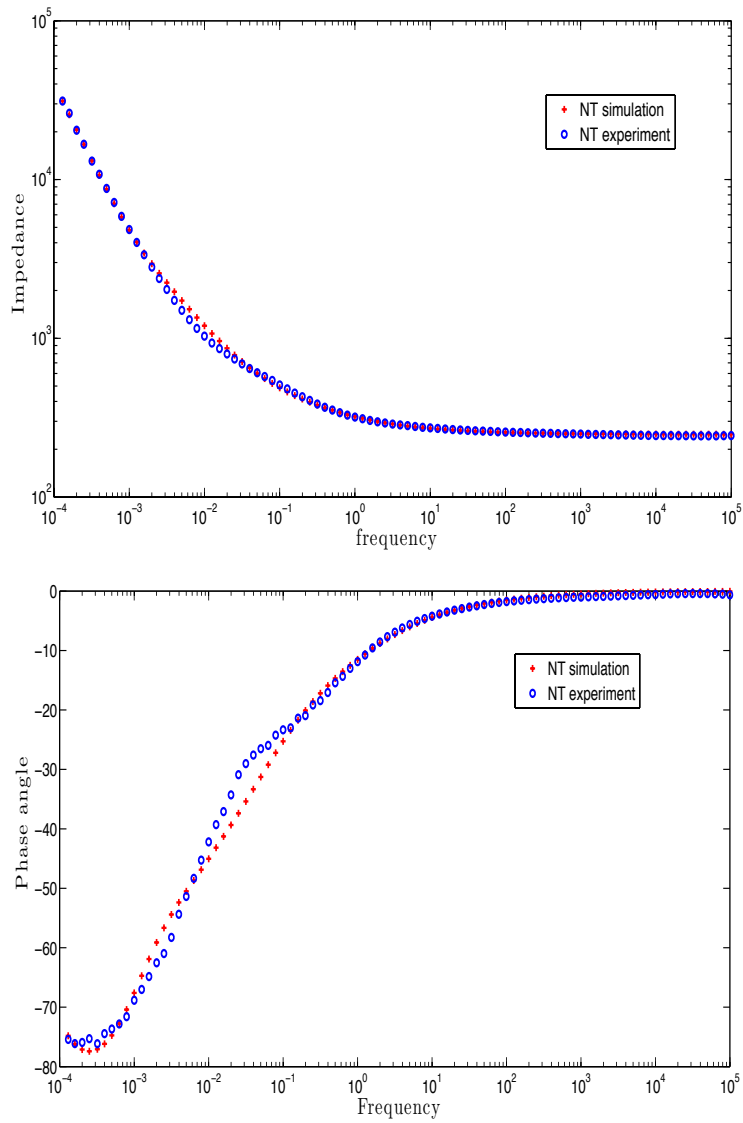


Figure 4.7: The Bode plot of the NT electrode.

itance, ionic resistance, faradaic resistance, solution resistance, paper resistance, and thickness variation of the electrode are varied, starting with the experimentally determined values shown in Table 4.2. It has been found that capacitance

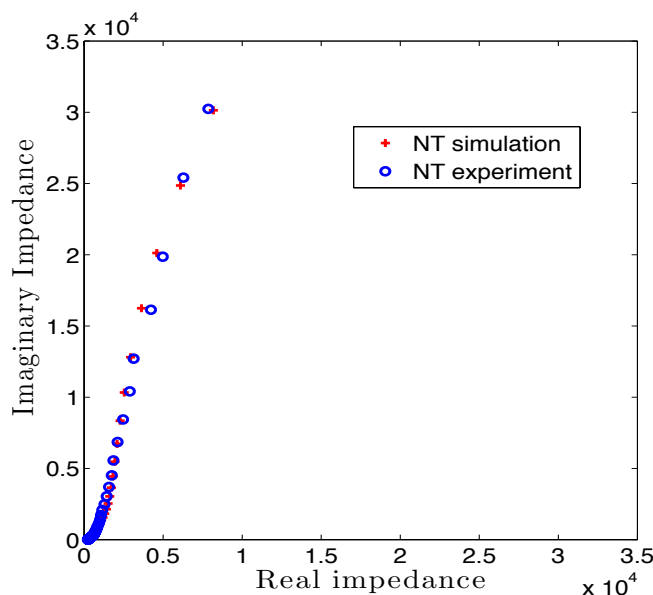


Figure 4.8: The Nyquist plot of the NT electrode.

and thickness variation are the main factors determining the capacitive transition response and the ionic resistance is a dominant factor at frequency range 10^{-1} Hz - 10^2 Hz. First, the NT electrode fitting is shown in Figure 4.7 - 4.8. It demonstrates good fitting over the entire frequency range on both the Bode and the Nyquist plot. This is believed to demonstrate that the distributed thickness variation may be the physical origin of the time constant distributed response in the electrochemical impedance measurement.

The multiple time constant model of the WT electrode is compared to the EIS experimental data in Figures 4.9 - 4.10. The phase angle of the WT simulation shows slightly different capacitive transition than the experiment. This suggests

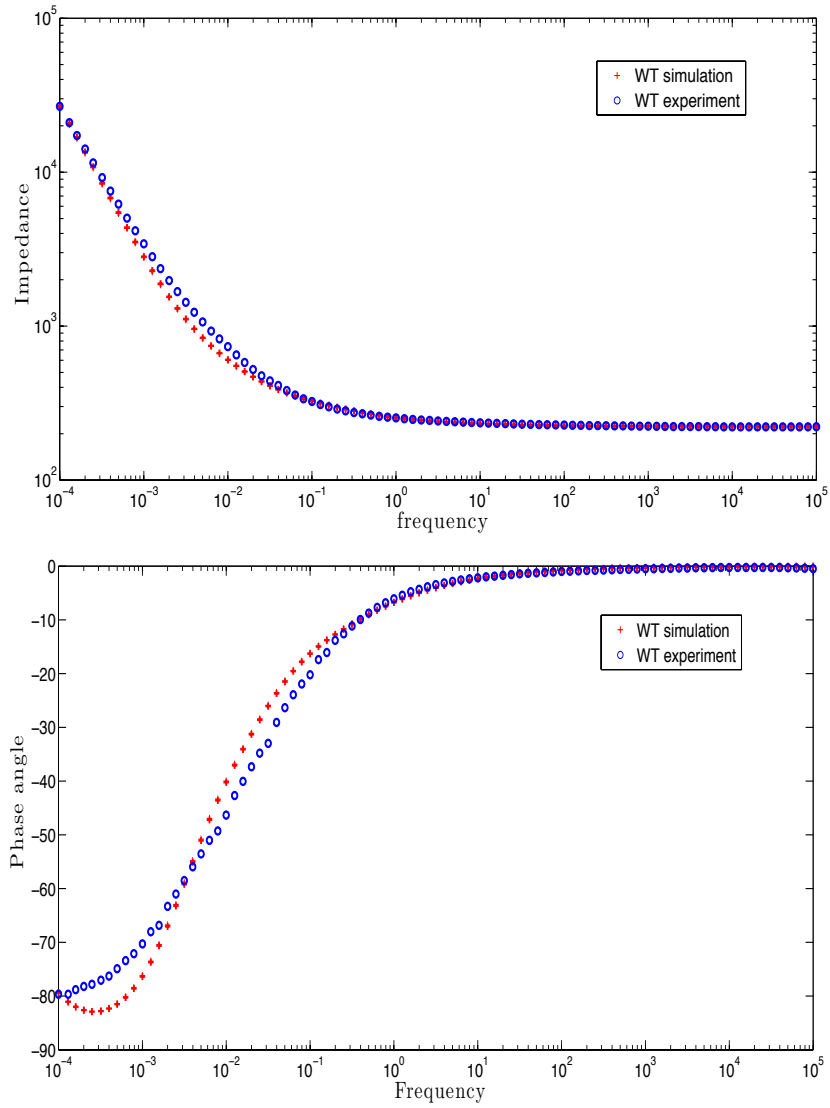


Figure 4.9: The Bode plot of the WT electrode.

that the WT electrode has a capacitance distribution that is governed by more factors than just the distribution of thickness.

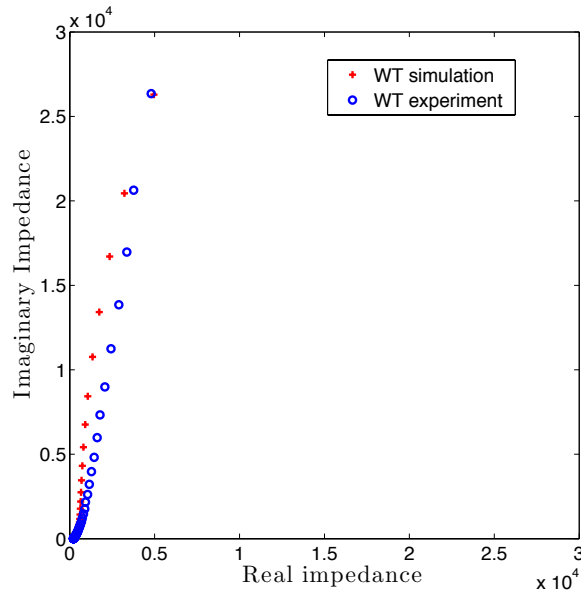


Figure 4.10: The Nyquist plot of the WT electrode.

The thickness is the primary parameter determining the total resistance and capacitance of an RCTL. However, the measured thickness variation did not fully explain the frequency dispersion for WT electrode. In order to find the effect of the highly distributed resistances and capacitances, a lognormal distribution function (LNDF) is employed, i.e., different standard deviations of the thickness can control the capacitance and ionic resistance distribution in the electrode. The thickness of the 20 x 10 sections is distributed with LNDF instead of using the actual measured thickness. Data fitting with different sigma values demonstrate results consistent with experimental reports [39]-[40], i.e., the distribution of the capacitance determines the slope of the capacitive transition. The multiple time constant modelling with LNDF demonstrates almost identical fitting at with the

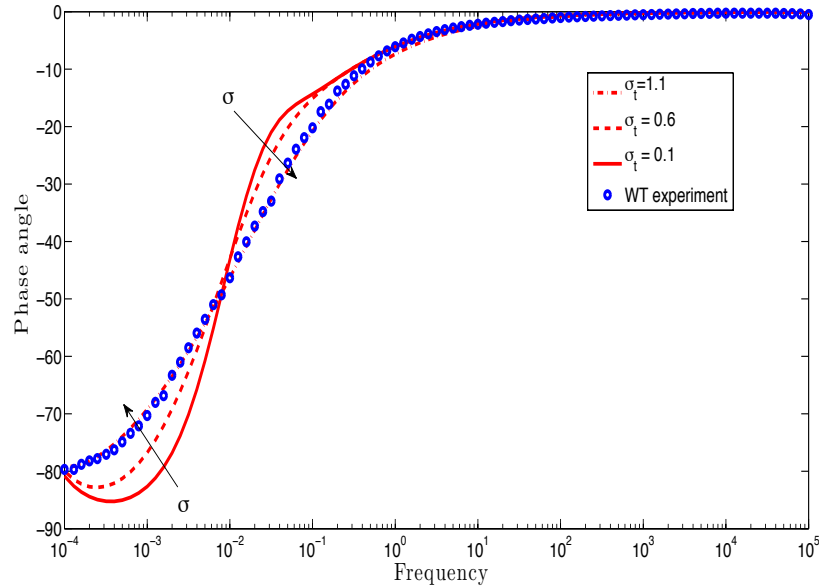


Figure 4.11: Phase angle response with different σ_t values.

EIS experimental result at a high standard deviation ($\sigma_t = 1.1$). This suggests that the thickness variation is not the only factor leading to increase in capacitance distribution of the PEDOT:PSS electrode. We need more detailed investigation to find out the cause of the distributed R_i and C . However, the effect of the Triton X-100 can be the cause for the distributed R_i and C . There are no research reports of the Triton X-100 effect on the morphology of the PEDOT:PSS electrode. However, if increased porosity is a local effect, R_i and C values in that region will be much lower than other area. Therefore, the addition of Triton X-100 can increase the distribution of resistance and capacitance values.

By comparing simulation results of different sigma values, it also has been

found that the capacitance distribution is a limiting factor of capacitor charging. As shown in Figure 4.11, the simulation with high sigma takes more time to charge the capacitor, i.e., capacitor charging time and σ_i has an inverse proportional relationship.

Table 4.2: Experiment and modelling data comparison. C , σ_i , R_s , and R_f refer to the capacitance, ionic conductivity, solution resistance, and faradaic resistance respectively.

Sample	C (F)	σ_i (S/m)	R_s (Ω)	R_f (Ω)
WT simulation	0.058	$2.32 \cdot 10^{-4}$	305	$1.8 \cdot 10^5$
WT experiment	0.075	$2.57 \cdot 10^{-4}$	N/A	N/A
NT simulation	0.039	$1.13 \cdot 10^{-4}$	330	$1.5 \cdot 10^5$
NT experiment	0.054	$1.04 \cdot 10^{-4}$	N/A	N/A

All the parameter values used in fitting are compared to the experimental results in Table 4.2. The capacitance used in the simulation of both WT and NT electrodes show lower value than the experimental result. The capacitance of the connector, which is not included in simulation, can induce this difference in capacitance between experiment and simulation. The ionic conductivities (σ_i) for both WT and NT electrode which are used in simulation show good agreement with experiment because of the realistic ion penetration mechanism employed in the modelling. The solution resistances (R_s) of 305 Ω (WT), 330 Ω (NT) are used for simulation. Unlike the solution resistance measurement apparatus (Figure 3.3), in the electrochemical impedance measurement (Figure 3.8), the ion transport paths are not restricted and thus simple comparison between simulation data and experiment data is not relevant. Therefore, the only simulation data is described in

Table 4.2. We believe that the experimental variation of positioning WE and RE contributed to the differences in resistance between WT and NT samples.

The multiple time constant model is constructed based on the theories [39]-[40] that explain physical origin of the CPE response as a capacitance distribution. Thickness variation of the PEDOT:PSS electrode is assumed as a primary reason for the CPE response and thus actual thickness variation is incorporated in the modelling. The NT electrode demonstrated good fitting through out the whole frequency range. It suggests that the thickness variation can be the main cause of the capacitance distribution of the PEDOT:PSS electrode. Unlike the NT simulation, the WT fitting suggests that there are more causes of the capacitance distribution than just the thickness. We need further investigation to determine the cause. However Triton X-100 is the most probable origin for the capacitance distribution. If the increased porosity of the WT electrode is not uniform, capacitor charge time will be different locally and it can also cause the capacitance distribution.

It has been shown that the distributed capacitances combined with ionic conductivities are the rate limiting mechanism for supercapacitor charging in Figure 4.11. The addition of the Triton X-100 decreases the thickness variation. However, data fitting suggests that the increased porosity caused by the addition of Triton X-100 might also induce capacitance distribution. In chapter 3, we described that the addition of Triton X-100 can improve charging speed but it is not

improving capacitance itself. However, considering that the ideal charging time for supercapacitors are between $10^{-2} - 10^2$ s [43], addition of Triton X-100 is better in practical applications.

Chapter 5

Conclusions

In this thesis, a flexible supercapacitor is fabricated with micropatterning technology and charge/discharge response is measured and simulated in order to understand the rate limiting mechanisms and assess its value. In contrast to the initial purpose of the Triton X-100; i.e., increase the PEDOT:PSS solution adhesion to the substrate, the addition of the surfactant also demonstrated higher volume capacitance at fast and intermediate scan rates (10 mV/s - 1 mV/s). Increased porosity of the PEDOT:PSS electrode is the cause of the faster capacitor charging effect. The ionic conductivity measurements have been performed to validate the hypothesis of increased porosity in the WT electrode.

In order to investigate the rate limiting factors of capacitor charging, electrochemical impedance measurements and equivalent circuit modelling are utilized. A frequency dispersive response that cannot be explained by simple arrangements

of electrical elements such as resistors, capacitors, or inductors is observed in EIS measurements. Among various theories explaining the physical origin of the frequency dispersive responses, multiple time constant modelling is constructed based on the theories that explain physical origin as a capacitance distribution.

Thickness variations are measured and incorporated in a multiple time constant modelling which consists of 200 parallel RC transmission lines. The basic concept of this modelling is ions will take more or less time to charge the capacitors if the thickness is varying throughout the electrode. Therefore, unlike the simple equivalent circuit modelling, this multiple time constant modelling demonstrates the time constant dispersive behaviour.

Thickness variation did not fully explain the frequency dispersion in sample with Triton X-100. However, sample without Triton X-100 demonstrated good agreement between experiment and simulation which can be explained with more highly distributed thickness distribution. A lognormal distribution function (LNDF) is utilized in order to investigate the relationship between the capacitance distribution and the capacitor charging, i.e., different standard deviations of time constant can control the capacitance distribution in the electrode. A good data is demonstrated at high standard deviation ($\sigma_t = 1.1$), which suggests that there are more factors distributing capacitances than just thickness distribution. By comparing simulation results of different sigma values, it has been found that the capacitance distribution is also a capacitor charge limiting factor along with

total capacitance.

The thickness measurements and data fitting suggested two effects of the Triton X-100. The Triton X-100 decreases the thickness variation of the PEDOT:PSS electrode. However, the data fitting suggests that there might be additional capacitance distribution caused by the addition of Triton X-100. The comparison with the sample without Triton, the WT electrode demonstrates substantial charging speed improvement at high scan rates (10 mV/s) and still faster charging speed at intermediate scan rates (1 mV/s). Therefore, considering ideal charging time for supercapacitors ($10^{-2} - 10^2$ s), addition of Triton X-100 is beneficial in practical applications.

There are research reports which already demonstrated experimentally that the distributed capacitance is the physical cause of the time constant distributed behaviour in electrochemical impedance measurement. However, there was no analytical modelling supporting these experimental results. This is the first analytical model showing that the capacitance distribution of the electrode is the main cause of the time constant distributed response. In addition to the measured thickness variation, comparison results of main parameters (capacitance, and ionic conductivity) used in multiple time constant modelling and experiment results also suggest that this multiple constant model is explaining the real cause of the time constant distributed response.

Bibliography

- [1] J. P. Zheng and T. R. Jow, "High energy and high power density electrochemical capacitors," *Power Sources*, vol. 62, pp. 155-159, 1996. → pages 2
- [2] A. Chu and P. Braatz, "Comparison of commercial supercapacitors and high-power lithium-ion batteries for power-assist applications in hybrid electric vehicles: I. Initial characterization," *Power Sources*, vol. 112, pp. 236-246, 2002. → pages 2
- [3] J. Chmiola *et al.*, "Anomalous Increase in Carbon Capacitance at Pore Sizes Less Than 1 Nanometer," *Science*, vol. 313, pp. 1760-1763, 2006. → pages 6
- [4] Celine Largeot *et al.*, "Relation between the Ion Size and Pore Size for an Electric Double-Layer Capacitor," *J. Am. Chem. Soc.*, vol. 130, pp. 2730-2731, 2008. → pages 6
- [5] Andrew Burke, "R&D considerations for the performance and application of

- electrochemical capacitors,” *Electrochimica Acta.*, vol. 53, pp. 1083-1091, 2007. → pages 6, 7
- [6] A. V. Rosario *et al.*, “Investigation of pseudocapacitive properties of RuO₂ film electrodes prepared by polymeric precursor method,” *Power Sources*, vol. 158, pp. 795-800, 2006. → pages 7
- [7] H. Zhou *et al.*, “The effect of the polyaniline morphology on the performance of polyaniline supercapacitors,” *Solid State Electrochem.*, vol. 9, pp. 574-580, 2005. → pages 7
- [8] K. R. Prasad and N. Munichandraiah, “Fabrication and evaluation of 450 F electrochemical redox supercapacitors using inexpensive and high-performance, polyaniline coated, stainless-steel electrodes,” *Power Sources*, vol. 112, pp. 443-451, 2002. → pages 7
- [9] E. Frackowiak and F. Beguin, “Carbon materials for the electrochemical storage of energy in capacitors,” *Carbon*, vol. 39, pp. 937-950, 2001. → pages 6
- [10] R. Kotz and M. Carlen, “Principles and applications of electrochemical capacitors,” *Electrochimica Acta.*, vol. 45, pp. 2483-2498, 2000. → pages vii, 8, 9
- [11] D. A. Scherson and A. Palencsar, “Batteries and Electrochemical Capacitors,” *The Electrochemical Society Interface*, 2006. → pages vii, 8

- [12] S. Pay *et al.*, “Effectiveness of Battery-Supercapacitor Combination in Electric Vehicles,” *IEEE Bologna Power Tech Conference*, June 23th - 26th, Italy, 2003. → pages 9
- [13] X. Li *et al.*, “Surface modification of polyaniline using tetraethyl orthosilicate,” *Colloid and Interface Science*, vol. 322, pp. 429-433, 2008. → pages 13, 16
- [14] K. S. Ryu *et al.*, “Symmetric redox supercapacitor with conducting polyaniline electrodes,” *Power Sources*, vol. 103, pp. 305-309, 2002. → pages 13, 16
- [15] P. Glynn-Jones *et al.*, “A feasibility study on using inkjet technology, micropumps, and MEMs as fuel injectors for bipropellant rocket engines.” University of Southampton, UK, SO17 1BJ → pages 13
- [16] J. Brunahl and A. M. Grishin, “Piezoelectric shear mode drop-on-demand inkjet actuator,” *Sensors and Actuators*, vol. 101, pp. 371-382, 2002. → pages 13
- [17] H. Sirringhaus *et al.*, “High-Resolution Inkjet Printing of All-Polymer Transistor Circuits,” *Science* vol. 290, pp. 2123-2126, 2000. → pages 14
- [18] S. E. Burns *et al.*, “Inkjet Printing of Polymer Thin-Film Transistor Circuits,” *Material Research Society*, 2003. → pages 14
- [19] M. J. Heller, “DNA MICROARRAY TECHNOLOGY: Devices, Systems,

- and Applications,” *Annu. Rev. Biomed. Eng.*, vol. 4, pp. 129-153, 2002. → pages 14
- [20] A. V. Lemmo *et al.*, “Inkjet dispensing technology: applications in drug discovery,” *Current opinion in biotechnology*, vol. 9, pp. 615-617, 1998. → pages 14
- [21] A. Bietsch *et al.*, “Rapid functionalization of cantilever array sensors by inkjet printing,” *Nanotechnology*, vol. 15, pp. 873-880, 2004. → pages 15
- [22] M. Kaempgen *et al.*, “Printable Thin Film Supercapacitors Using Single-Walled Carbon Nanotubes,” *Nano Letters*, vol.9, pp. 1872-1876, 2009. → pages 15
- [23] D. Pech *et al.*, “Elaboration of a microstructured inkjet-printed carbon electrochemical capacitor,” *Power Sources*, vol. 195, pp. 1266-1269, 2010. → pages 15
- [24] P. Gajendran and R. Saraswathi, “Polyaniline-carbon nanotube composites,” *Pure Appl. Chem.*, vol. 80, pp. 2377-2395, 2008. → pages 16
- [25] M. H. Tsai *et al.*, “Effects of pulse voltage on inkjet printing of a silver nanopowder suspension,” *Nanotechnology*, vol. 19, 2008. → pages 17
- [26] A. U. Chen and O. A. Basaran, “A new method for significantly reducing drop radius without reducing nozzle radius in drop-on-demand drop production,” *Physics of Fluids*, vol. 14, pp. L1-L4, 2002. → pages 17

- [27] T.C. Girija, M.V. Sangaranarayanan, "Polyaniline-based nickel electrodes for electrochemical supercapacitors Influence of Triton X-100," *Power Source*, vol. 159, pp. 1519-1526, 2006. → pages 25
- [28] S. Devaraj and N. Munichandraiah, "The Effect of Nonionic Surfactant Triton X-100 during Electrochemical Deposition of MnO₂ on Its Capacitance Properties," *Electrochemical Society*, vol. 154, pp. A901-A909, 2007. → pages 25
- [29] H. Yanazawa *et al.*, "Precision Evaluation in Kr Adsorption for Small BET Surface Area Measurements of Less Than 1 m²," *Adsorption*, vol. 6, pp. 73-77, 2000. → pages 26
- [30] V. Subramanian *et al.*, "Mesoporous anhydrous RuO₂ as a supercapacitor electrode material," *Solid State Ionics*, vol. 175, pp. 511515, 2004. → pages 31
- [31] Jeffrey W. Long *et al.*, "Voltammetric Characterization of Ruthenium Oxide-Based Aerogels and Other RuO₂ Solids: The Nature of Capacitance in Nanostructured Materials," *Langmuir*, vol. 15, pp. 780-785, 1999. → pages
- [32] J.H. Chen *et al.*, "Electrochemical characterization of carbon nanotubes as electrode in electrochemical double-layer capacitors," *Carbon*, vol. 40, pp. 1193-1197, 2002. → pages 31
- [33] J. Bisquert *et al.*, "Impedance of constant phase element (CPE)-blocked dif-

- fusion in film electrodes,” *Electroanalytical Chemistry*, vol. 452, pp. 229-234, 1998. → pages 35, 38
- [34] H. E. Brouji *et al.*, “Analysis of the dynamic behaviour changes of supercapacitors during calendar life test under several voltages and temperatures conditions,” *Microelectronics Reliability*, vol. 49, pp. 1391-1397, 2009. → pages 43
- [35] P. J. Mahon *et al.*, “Measurement and modelling of the high-power performance of carbon-based supercapacitors,” *Power Sources*, vol.91, pp. 68-76, 2000. → pages 43
- [36] H. K. Song *et al.*, “Electrochemical impedance spectroscopy of porous electrodes: the effect of pore size distribution,” *Electrochimica Acta.*, vol. 44, pp. 3513-3519, 1999. → pages 44, 49
- [37] G. J. Lee *et al.*, “Kinetics of double-layer charging/discharging of the activated carbon fiber cloth electrode: effects of pore length distribution and solution resistance,” *Solid State Electrochem.*, vol. 8, pp. 110-117, 2004. → pages 44, 49
- [38] M. Eikerling *et al.*, “Optimized Structure of Nanoporous Carbon-Based Double-Layer Capacitors,” *Electrochemical Society*, vol. 152, pp. E24-E33, 2005. → pages 44
- [39] C. H. Kim *et al.*, “An investigation of the capacitance dispersion on the frac-

- tal carbon electrode with edge and basal orientations,” *Electrochem Acta.*, vol. 48, pp. 3455-3463, 2003. → pages 45, 60, 63
- [40] Z. Kerner *et al.*, “On the origin of capacitance dispersion of rough electrodes,” *Electrochem Acta.*, vol. 46, pp. 207-210, 2000. → pages 46, 60, 63
- [41] G. F. Wang *et al.*, “Modification of Conductive Polymer for Polymeric Anodes of Flexible Organic Light-Emitting Diodes,” *Nanoscale Res. Lett.*, vol. 4, pp. 613-617, 2009. → pages 46
- [42] D. Soltman and V. Subramanian, “Inkjet-Printed Line Morphologies and Temperature Control of the Coffee Ring Effect,” *Nano Letters*, vol. 24, pp. 2224-223, 2008. → pages 46
- [43] R. Kotz and M. Carlen, “Principles and applications of electrochemical capacitors,” *Electrochimica Acta.*, vol. 45, pp. 2483-2498, 2000. → pages 64

Appendices

Appendix A

Design of the printing nozzle housing

We purchased inkjet printing equipment from Microdrop technologies (so called Microdrop system, German). However the design of the inkjet printing nozzle has a disadvantage, i.e., the glass orifice is not visible from the outside thus it was difficult to clean the clogged nozzle. The nozzles are also very expensive. Thus we designed custom inkjet printing nozzle housing by purchasing and integrating MJ-ABP-01 single jet dispensing nozzle (from Microfab Technologies company, USA). The nozzle assembly and complete nozzle housing is shown in Figure A.1. Microfab nozzles are compatible with the Microdrop system. However, the Microdrop system is designed for a nozzle of resistance $2.6\text{M}\Omega$, whereas the resistance of the Microfab nozzle is lower ($1.53\text{M}\Omega$). Therefore, attention needs to be paid when it is used over 100V to prevent component failure of the

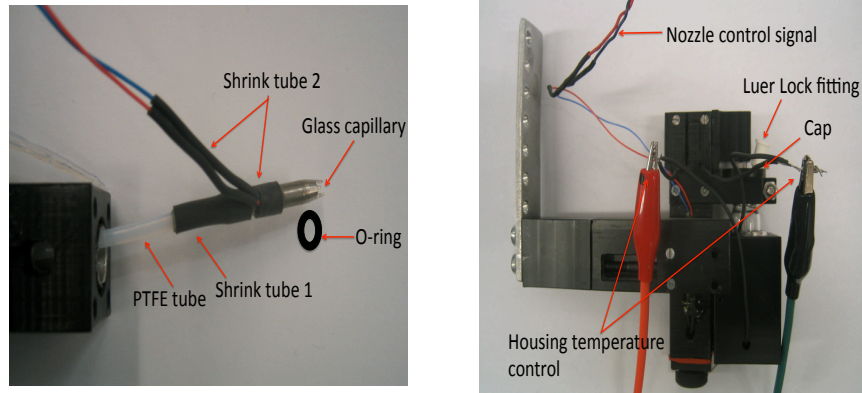


Figure A.1: Design and assembly of the inkjet printing nozzle housing.

piezo drive system.

Chemically non-reactive PTFE is chosen for the tubing material. However, it is often observed that the connection between nozzle and PTFE tube are weakened and disconnected due to the high air pressure which is used to clean the clogged nozzle. In order to prevent the PTFE tube from disconnecting, inner adhesive shrink tube is used as shown in Figure A.1 - shrink tube 1. The adhesion layer of the shrink tube prevents disconnection during the cleaning process. The shrink tube is also used to prevent wire disconnection and scratching from the assembly process (Figure A.1 - shrink tube 2). The O-ring is added to the tip of nozzle to prevent water from getting inside the housing as well as fix the position of nozzle (FigureA.1 - O-ring). It is important not to soak the housing body even with this O-ring shielding. Luer lock fitting is used to connect the air pressure supply to the

nozzle housing (Figure A.1 - Luer Lock fitting). In order to get a pressure leak free connection, the thread of the luer lock fitting is wrapped with PTFE film tape. The tube path hole is made smaller to ensure pressure leak free assembly. 1.8 mm hole is designed to the cap with 2.38 mm diameter PTFE tube. The larger tube is squeezed inside the cap without any problems.

Appendix B

Nozzle maintenance tips

Cleaning a clogged nozzle is quite a time consuming task when we are using inkjet printing system. Here, two practical tips are shared to clean a clogged nozzle. First, the vacuum backflush can be an effective approach to remove any loose clog. The clogged nozzle tip should be immersed in a solvent. The strong backward stream with solvent can rapidly remove particles. The pressure control unit (AD-E-130) of the Microdrop system can be used to apply vacuum to the nozzle. The other method involves the use of a low power ultrasonicator with nitrogen gas and solvent. It is often observed that dust moves inside the nozzle after sonication. However, the dust clogs the nozzle tip again when it is used later. By applying low gas pressure to the clogged nozzle, we can cause constant solvent flow through the tip and this helps to maintain the dust position during sonication. In order to avoid damaging the electrical connection part, we should be careful not to immerse the whole nozzle into the sonication bath.